Anthropogenic carbon storage and its decadal changes in the Atlantic 1990–2020

Reiner Steinfeldt[1], Monika Rhein[2], and Dagmar Kieke[1,2,3]

[1]Institute of Environmental Physics, University of Bremen, Bremen, Germany
[2]MARUM - Center for Marine Environmental Sciences, University of Bremen, Bremen, Germany
[3]now at Federal Maritime and Hydrographic Agency (BSH), Hamburg, Germany

Correspondence: Reiner Steinfeldt (rsteinf@physik.uni-bremen.de)

Abstract. The Atlantic inventory of anthropogenic carbon (C_{ant}) and its changes between 1990 and 2020 are investigated by applying the transit time distribution (TTD) method to anthropogenic tracer data. In contrast to previous TTD applications, here we take into account the admixture of old waters free of anthropogenic tracers. The greatest difference to other methods based on direct carbon observations is the higher C_{ant} storage in the deep ocean. The results from the TTD method better reflect the observed distribution of other transient tracers such as chlorofluorocarbons (CFCs). Changes in oceanic circulation/ventilation are important on the regional scale. The enhanced upwelling of older water in the Southern Ocean and the decline in the convection depth in the Labrador Sea lead to deviations of the inferred C_{ant} increase between 1990 and 2020 from the rate equivalent to a steady state ocean. For the total Atlantic C_{ant} inventory, however, decadal ventilation variability of individual water masses is partially compensating each other. In addition, its impact on the C_{ant} storage is small due to the much higher flushing time for the total Atlantic of the order of hundreds of years. The total C_{ant} inventory increases from $43.0 \pm 7.3 \, \mathrm{Pg\,C}$ in 1990 to $68.2 \pm 10.8 \, \mathrm{Pg\,C}$ in 2020, almost in unison with the rising CO_2 in the atmosphere. So far, ventilation changes have impacted the C_{ant} concentrations only on the regional scale.

1 Introduction

The ocean is an important sink for anthropogenic carbon (C_{ant}) emissions from e. g. fossil fuel burning, cement production and land use change (*Friedlingstein et al.*, 2020). Over the industrial era, about 30 % of these emissions have been taken up by the ocean (*Gruber et al.*, 2019) (inferred from observations). Based on global biogeochemical models that meet observational constraints, *Friedlingstein et al.* (2020) find a slightly smaller ocean carbon uptake of about $25\,\%$ of the emissions over the last decades. A small decrease ($< 5\,\%$) in the fraction of the CO_2 emissions taken up by the ocean is to be expected due to the decreasing buffer capacity of the oceanic waters. In addition, a slower oceanic circulation and mixing in a warming climate might reduce the uptake rate of surface waters for human-produced carbon (*Heinze et al.*, 2015). Future changes in the oceanic circulation may also alter the biological carbon pump and the storage of remineralized carbon (*Heinze et al.*, 2015).

The North Atlantic is the region with the highest column inventory of anthropogenic carbon (or the highest storage rates), both in models and observations (*Sabine et al.*, 2004; *Khatiwala et al.*, 2013). It is also a region with large variability in water mass formation, especially for Labrador Sea Water (*Kieke et al.*, 2006; *Rhein et al.*, 2007; *Yashayaev*, 2007; *Kieke and*

Yashayaev, 2015; *Yashayaev and Loder*, 2016). These changes in water mass formation/ventilation also have an impact on the inventories of C_{ant} (*Steinfeldt et al.*, 2009; *Pérez et al.*, 2013; *Rhein et al.*, 2017). Our study addresses these impacts. In particular, it comprises the time frame with deep and intense formation of Labrador Sea Water (1987–1995), the following period of weaker convection (1996–2013) (*Kieke et al.*, 2007; *Yashayaev*, 2007; *Kieke and Yashayaev*, 2015) as well as the recent reinvocation of deep reaching convection since 2014, accompanied with an increase in C_{ant} uptake and oxygen concentrations (*Rhein et al.*, 2017).

C_{ant} in the ocean cannot be measured directly, but has to be inferred by indirect techniques. One group of methods to calculate C_{ant} concentrations are the so called "back calculation techniques", (e. g. ΔC^* (*Gruber et al.*, 1996), φC_T^0 (*Vázquez-Rodríguez et al.*, 2009)). These rely on measurements of dissolved inorganic carbon (DIC), the assumed natural background concentration of DIC, and the DIC originating both from the remineralization of organic matter and the dissolution of calcium carbonate. Another technique is the extended multiple linear regression (eMLR) (*Friis et al.*, 2005). Here, observations at two times of both DIC and auxiliary quantities such as temperature, salinity, nutrients and oxygen are needed, which allow to build a regression for DIC based on the other variables. By this method, only the difference in C_{ant} between the two dates can be determined, but not the absolute value. Recently, *Clement and Gruber* (2018) developed an eMLR for C^*, i. e. the observed DIC excluding the carbon from remineralization of organic matter and dissolution of calcium carbonate. This eMLR(C^*) method has also been applied by *Gruber et al.* (2019) and *Müller et al.* (2023) to the observational data from the GLODAPv2 data set (*Lauvset et al.*, 2024).

Other methods do not rely on directly measured carbon data. Instead, they take advantage of anthropogenic tracers like CFCs and SF_6 and lead to C_{ant} distributions more compatible to these tracers. These methods are the transit time distribution (TTD) method (*Hall et al.*, 2002; *Waugh et al.*, 2006) and the Green's function (GF) approach (*Holzer and Hall*, 2000; *Khatiwala et al.*, 2013). They consider C_{ant} as a passive tracer that is advected from the surface into the ocean interior. Thus, these methods do not require to make assumptions about the biochemical involvement of carbon (the biological pump) as necessary for the aforementioned methods. On the other hand, they need to make assumptions of the temporal evolution of C_{ant} in the mixed layer of the ocean and the shape of the TTD or Green's function. Another advantage of the TTD technique – which will be exploited here – is to make predictions of C_{ant} concentrations from older observations - under the assumption that the ocean is in steady state. This allows to distinguish wether C_{ant} changes between two time period (i) originate from the atmospheric CO_2 increase or (ii) are caused by changes in the ocean circulation.

The different C_{ant} calculation methods lead in general to inventory differences of the order of $\pm 10\%$, both on the global scale (*Khatiwala et al.*, 2013) as well as along basin-wide sections in the Atlantic (*Vázquez-Rodríguez et al.*, 2009). However, the vertical distribution of the inventory is different, with the ΔC^* method attributing a smaller fraction to the deep water masses (*Vázquez-Rodríguez et al.*, 2009). This holds also for recently ventilated deep and bottom waters. On the regional scale, the inventory differences are larger, especially in the Southern Ocean (*Vázquez-Rodríguez et al.*, 2009). For the biogeochemical consequences of oceanic C_{ant} storage like ocean acidification, not only the total oceanic C_{ant} uptake, but also its local storage rates as well as the vertical distribution are of importance.

Table 1. List of used cruises with transient tracer data not included in GLODAPv2.2023.

Cruise	Year	Data Availability
JC057[a]	2011	https://www.bodc.ac.uk/geotraces/data/idp2017/
MSM64	2017	https://doi.org/10.1594/PANGAEA.962044
MSM73	2918	https://doi.org/10.1594/PANGAEA.962113

[a]Part of GEOTRACES section GA02

Here, we use a modified version of the TTD method to infer the inventories of C_{ant} over the Atlantic from $70°S$ to $65°N$
for the years 1990, 2000, and 2010. The method is mainly based on *Steinfeldt et al.* (2009), but additionally allows for the
admixture of old waters free of anthropogenic tracers. The impact of this modification of the TTD method on the derived C_{ant}
concentrations will be described. We will then quantify the decadal C_{ant} inventories and their changes and compare them with
a steady state ocean, where C_{ant} is solely changing due to the rising atmospheric CO_2 concentration. This allows to quantify
the impact of changes in ocean ventilation and circulation on C_{ant}, i. e. the main processes storing C_{ant} in the ocean interior.
We further discuss our results with respect to so far existing global studies and highlight and discuss prominent similarities and
discrepancies.

2 Data and Methods

2.1 Data and calculation of C_{ant} distributions

We use anthropogenic tracers (CFC-12, CFC-11, CFC-113, tritium and SF_6) to calculate transit time distributions (TTDs),
from which finally the concentration of C_{ant} is inferred. The data is mainly taken from the GLODAPv2.2023 data product
released in 2023 (*Lauvset et al.*, 2024). The transient tracer data discussed here cover the time between 1982 and 2021. Also
the GEOTRACES GAO2 section from 2010/2011 (*Schlitzer et al.*, 2018) and data from North Atlantic cruises conducted over
the period 2017–2018 and not contained in this data product have been added here (Table 1). The salinity and transient tracer
data of these additional cruises have been underwent similar bias control procedures as those in the GLODAPv2.2023 data
product, and no offset could be detected.

The data are grouped into four periods roughly centered around 1990, 2000, 2010 and 2020. These time segments include
the years 1982–1994, 1995–2005, 2006–2013 and 2014–2021 respectively. The periods are chosen to allow for a good data
coverage of the Atlantic at least for the first three periods. For the time frame 2014–2021, the data are sparse except for the
North Atlantic. The main focus for the last period is to investigate the effect of the reinvocation of deep convection in the
Labrador Sea (*Yashayaev and Loder*, 2016) on the C_{ant} distribution. Table 2 shows the number of available tracer data for the
four periods. The location of all profiles with CFC-12 and/or CFC-11 data for every decade are indicated in Fig. 1a–d. Tritium,
CFC-113 and SF_6 are colocated with CFC-11/CFC-12, but have much lesser data points. They are mainly used to infer the
shape of the TTD (see section 2.3.1) for the whole time period.

Table 2. Number of anthropogenic tracer samples used for the C_{ant} calculation.

Time period	Number of samples			
	CFC-12 or CFC-11	SF$_6$	CFC-113[a]	Tritium[a]
1982–1994	41,301	0	5,242	1,145
1995–2005	79,888	2,522	26,955	581
2006–2013	42,349	18,806	6,573	0
2014–2021	14,010	14,162	0	23

[a]CFC-113 and tritium are only used to calculate the ratio of with Δ over mean age Γ of the TTDs, independent from time, see section 2.3.1
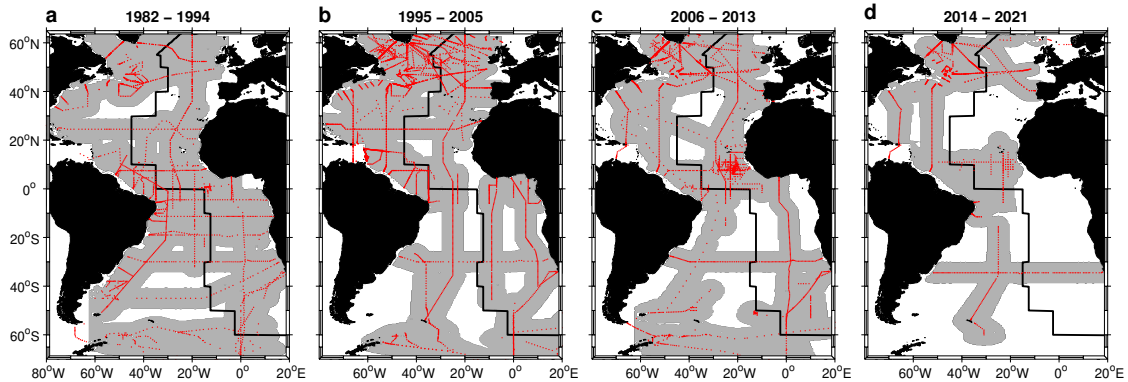
Figure 1. Location of ship stations with CFC-12 and/or CFC-11 data used for the C_{ant} calculation for the four decades considered here. a: 1982–1994, b: 1995–2005, c: 2006–2013, d: 2014–2021. The grey shaded area indicate the region for which gridded C_{ant} data could be generated for the respective period. The thick black line following the Mid-Atlantic Ridge is used for the separating the Atlantic Ocean into a western and eastern basin.

For the isopycnal interpolation of salinity, potential temperature and anthropogenic carbon, at each profile mean values over 38 density layers are calculated. The boundaries of these density intervals are given in table A1. For the upper layers, the potential density referenced to the surface is used (σ_θ), for the intermediate layers $\sigma_{1.5}$, referenced to $1500\,\mathrm{dbar}$, and for the deep layers σ_4, referenced to $4000\,\mathrm{dbar}$. At some locations, the deepest σ_θ layer is located below the upper $\sigma_{1.5}$ layers. In this case, these upper $\sigma_{1.5}$ layers remain empty. The same holds for the transition between $\sigma_{1.5}$ and σ_4. A mean value for a density layer is only calculated, if at least one data point is located within that density interval. Typically, the number of density levels for a deep reaching profile is about 30. The layers with the lightest densities only exist at low latitudes, and the densest σ_4 layers only in the AABW core and in the North Atlantic south of Denmark Strait.

The isopycnal mean values are then mapped horizontally (i. e. isopycycnally) on a regular grid ($0.5°$ longitude $\times 0.25°$ latitude) from $70°$S to $65°$N and $80°$W to $20°$E. As the number of available samples from the water bottles is typically around

20 per profile, some density layers might not get assigned a mean value. As these "empty" layers change from profile to profile, there are still enough points for each density layer to perform the gridding procedure.

The gridding method is similar to that applied in *Rhein et al.* (2015), i. e. an objective mapping scheme is used, where the weighting factor decreases with distance r from the data points ($\exp(-r^2)$). An additional weighting factor proportional to $\exp(-(\Delta(f/H))^2)$ (f: Coriolis parameter, H: water depth, $\Delta(f/H)$: difference in f/H between grid point and data point), which results in a terrain following interpolation, is only applied to the $\sigma_{1.5}$ and σ_4 density levels, as the upper lighter waters are less constrained by topography. The marginal seas like Mediterranean, Caribbean and North Sea are excluded from the gridded data.

Potential (σ_θ, $\sigma_{1.5}$ and σ_4) and neutral densities are vertically interpolated every $100\,\mathrm{m}$ and horizontally mapped in the same way as the other quantities. The gridded data of the potential densities are used to infer the thicknesses of the isopycnal layers. In addition to gridding the data for the periods 1982–1994, 1995–2005, 2006–2013 and 2014–2021, all data from the whole period 1982–2021 are pooled together to produce climatologies for density, salinity, potential temperature and C_{ant}. The gridded fields for the individual decades in some locations have gaps due to sparse input data (distance between grid point and data point $> 4.5°$ or roughly $500\,\mathrm{km}$, Fig. 1). This is not the case for the gridded climatological fields based on the entire data set. In these cases, the gaps of the respective decadal fields are filled by the values obtained from the climatology. For the periods 1982–1994 and 1995–2005, about $10\,\%$ of the decadal gridded values are missing, for the period 2006–2013, where the data gaps are larger, about $20\,\%$, and for the last period 2014–2021 with the largest data gaps less than $50\,\%$, see Fig 1. The data coverage is still good in the North Atlantic, and worst in the southern part and the northeastern suntropics. For this period we fill the data gaps not from the climatology, but from the previous decade. In this sense, the 2014–2021 C_{ant} data is an "update" of the 2006–2013 period, but potential changes especially in the South Atlantic might be underestimated. On the other hand, in the North Atlantic, where temporal variability of LSW ventilation does occur, the data coverage is sufficient to reproduce these changes.

From the gridded data we compute column inventories for C_{ant}. Therefor, the C_{ant} concentrations for each isopycnal layer are multiplied with the density and layer thickness, and then integrated vertically. This results in an inventory of C_{ant} per square meter. In addition, C_{ant} and salinity are studied along two meridional sections that represent zonal means over the western and eastern basin of the Atlantic. The separation line mainly follows the course of the Mid-Atlantic Ridge (see Fig. 1). Selected isopycnals of neutral density γ_n and potential temperature θ from the 'climatological' fields are also shown in the section plots to give a rough overview on the distribution/location of the main water masses as described below.

2.2 Major water masses and their definition

The distribution of C_{ant} is inevitably linked to the spreading of the different water masses. We thus give a short overview over the major water masses in the Atlantic. The zonal mean salinity sections for the western and eastern Atlantic indicate the position of the main water masses (Fig. 2). The areas with high salinities reaching down to $400-600\,\mathrm{m}$ depth between $20°S-40°S$ and $20°N-40°N$ belong to the Subtropical Mode Waters (STMW). These are formed in the subtropical gyres by buoyancy loss and subduction (*Talley*, 1999). Further north in the eastern basin, the upper few hundred meters are covered
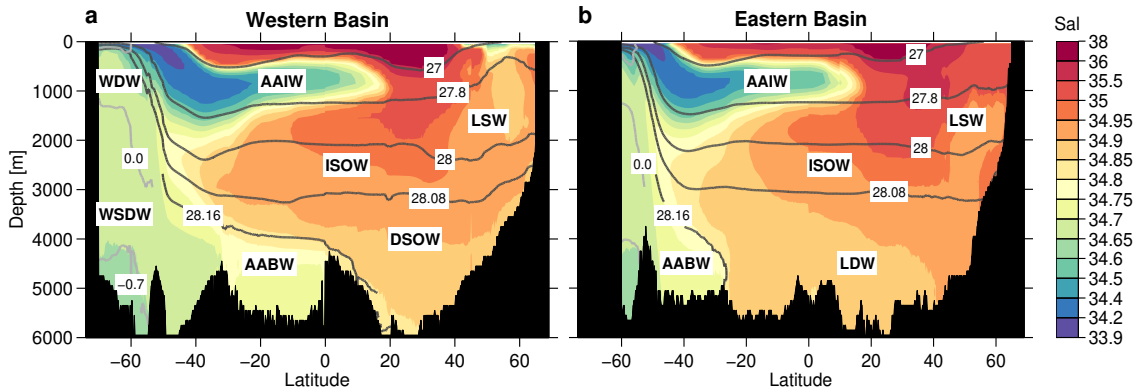
Figure 2. Zonal mean sections of salinity, a: western Atlantic basin, b: eastern Atlantic basin. Contour lines show zonally averaged neutral density isopycnals γ_n (dark grey) and isotherms (light grey, $\theta = 0.0\,^{\circ}$C and $\theta = -0.7\,^{\circ}$C, south of $50\,^{\circ}$S only) as boundaries of the main water masses. For acronyms of water masses see text.

by Subpolar Mode Water (SPMW) (*Brambilla and Talley*, 2008), which also has a relatively high salinity (> 35). The deeper region with salinities > 35.5 around $1000\,$m and $40\,^{\circ}$N in the eastern basin is dominated by the Mediterranean Outflow Water
130 (MOW). As can be seen from the salinity distribution, this water mass penetrates further into the western basin and also mixes into the underlying North Atlantic Deep Water (NADW).

The low salinity tongue at around $1000\,$m stretching from $45\,^{\circ}$S $- 20\,^{\circ}$N marks the Antarctic Intermediate Water (AAIW). This water mass is formed at the Subantarctic Front at about $45\,^{\circ}$S by ventilation of Subantarctic Mode Water (SAMW) formed in the southeast Pacific and Drake Passage (*McCartney*, 1982). It even reaches the subpolar North Atlantic, but loses its
135 characteristic salinity minimum (*Álvarez et al.*, 2004).

The most prominent deep water mass is the North Atlantic Deep Water, which consists of different components, i. e. Labrador Sea Water (LSW), Iceland-Scotland Overflow Water (ISOW) and Denmark Strait Overflow Water (DSOW). The LSW is formed in the northwestern subpolar North Atlantic, by deep convection, occasionally reaching down to $2000\,$m (*Lazier et al.*, 2023; *Yashayaev*, 2007; *Kieke and Yashayaev*, 2015). The salinity minimum associated with this newly formed LSW is clearly
140 seen in Fig. 2a between $50\,^{\circ}$N and $60\,^{\circ}$N. When spreading south- and eastward, the salinity of LSW increases due to mixing with surrounding more saline water masses, especially MOW.

The ISOW enters the subpolar North Atlantic via the Iceland-Scotland Ridge. It entrains ambient waters such as SPMW (*Mauritzen et al.*, 2005), which leads to the relatively high salinity of this water mass (see the salinity maximum in Fig. 2b at $60\,^{\circ}$N between $2000\,$m and $3000\,$m depth). Further downstream, the ISOW also entrains fresher LSW (*Dickson et al.*, 2002),
145 leading to a salinity decrease. Large parts of the ISOW enter the western basin mainly via the Charlie-Gibbs and the Bight Fracture Zones (*McCartney*, 1992; *Petit et al.*, 2018), while a smaller part continues southward in the eastern basin (*Fleischmann et al.*, 2001).

The densest component of NADW is the DSOW. South of Denmark Strait between Greenland and Iceland, this water spreads close to the bottom and entrains ambient waters (*Jochumsen et al.*, 2015). It is less saline than the ISOW above. Due to its high density and great depth (below $\approx 3500\,\mathrm{m}$), it cannot enter the eastern Atlantic directly.

In the Southern Ocean, NADW succumbs to upwelling and gets incorporated into the Circumpolar Deep Water (CDW) (*Iudicone et al.*, 2008). The southernmost extension of CDW between the Antarctic Continent and the Antarctic Circumpolar Current is called Warm Deep Water (WDW). This water also contains older deep water from the other oceans and more recently ventilated water from the Weddell Sea in the Atlantic Sector of the Southern Ocean (*Klatt et al.*, 2002).

The water mass close to the bottom with relatively low salinity is the Antarctic Bottom Water (AABW). In the Atlantic, AABW is formed in the Weddell Sea including subsurface excursions of saline shelf water below the ice shelf and substantial entrainment of WDW when descending into the abyss. It leaves the Southern Ocean guided by topography into the deep basins of the western Atlantic (*Bullister et al.*, 2013). Major pathways for deep and bottom waters to flow into the eastern basins are the Romanche Fracture Zone (*Mercier and Morin*, 1997) near the equator and the Vema Fracture Zone at $11°$N (*Fischer et al.*, 1996). This eastward penetration of AABW at the equator is visible by a salinity minimum directly above the bottom. The intensified vertical mixing with the overlying DSOW as observed in the Romanche Fracture Zone (*Mercier and Morin*, 1997) makes the bottom waters of the eastern basin more saline than in the western part. At the same time, the temperature increases and the density decreases. This altered AABW in the eastern basin is then called Lower Deep Water (LDW). The further salinity increase in the deep eastern Atlantic towards the northern boundary might be explained by intrusion of the densest part of ISOW. Nevertheless, the influence of AABW is still visible, e. g. by enhanced noble gas concentrations observed along $60°$N originating from the entrainment of subglacial melt water from the Antarctic ice shelves (*Rhein et al.*, 2018).

South of the fronts of the Antarctic Circumpolar Current, at about $55°$S, the densities of the deep water are considerably higher. There, the potential temperature θ is used to distinguish between Warm Deep Water (WDW, $\theta > 0\,°\mathrm{C}$) Weddell Sea Deep Water (WSDW, $0\,°\mathrm{C} > \theta > -0.7\,°\mathrm{C}$), and the Weddell Sea Bottom Water (WSBW, $\theta < -0.7\,°\mathrm{C}$ (*van Heuven et al.*, 2011)). WSBW, WSDW and WDW are precursor water masses of AABW.

The neutral density boundaries of some specific water masses are shown in all the section figures. We selected the boundaries according to the salinity distribution, i. e. the low salinity tongue of the AAIW is comprised by the isopycnals $\gamma_\mathrm{n} = 27.0\,\mathrm{kg\,m^{-3}}$ and $\gamma_\mathrm{n} = 27.8\,\mathrm{kg\,m^{-3}}$. For the NADW components, we roughly follow the values given in *Le Bras et al.* (2017). Only for the density at the lower boundaries of LSW and ISOW we use slightly denser isopycnals to better represent the salinity distribution. With the water mass boundaries shown in Fig. 2 the salinity minimum of the LSW in the northwest Atlantic and the salinity maximum of the ISOW at the northern boundary of the eastern basin are contained completely in the respective water mass. For the boundary between DSOW and AABW we have chosen the isopycnal $\gamma_\mathrm{n} = 28.16\,\mathrm{kg\,m^{-3}}$, almost following the isohaline $S = 34.85$. This leads to a northern boundary of AABW in the western basin at around $20°$N. There are some extensions of AABW found further north, but they have mixed with the overlying DSOW and are thus more saline and also more enriched in anthropogenic tracers.

2.3 Anthropogenic carbon inferred from the TTD method

In this paper, we use a modified TTD method to infer the concentration of C_{ant}. This is based on the method used in *Steinfeldt et al.* (2009). In addition, we explicitly allow for the admixture of old, tracer free waters. This approach has been used before, e. g. in *Steinfeldt and Rhein* (2004), but there it was locally restricted to the deep western boundary current in the tropics and was not used to calculate anthropogenic carbon. Here, we introduce a new algorithm that allows to assign the admixture of old water at any location.

2.3.1 The standard TTD method

First, we explain the standard TTD method by following the procedure in *Hall et al.* (2002). Due to the advective-diffusive nature of the oceanic transport, the water in the ocean interior consists of fluid elements with different pathways and ages (time elapsed since the water parcel left the mixed layer). The distribution of these ages τ is described by the TTD function $\mathcal{G}$. The concentration of any conservative property $C(\mathrm{x}, t)$ at location x in the ocean interior and time t, which can be a particular reference year t_{ref}, is then given by

$$C(\mathbf{x}, t_{\mathrm{ref}}) = \int\limits_0^\infty C^0(t_{\mathrm{ref}} - \tau)\, \mathcal{G}(\mathbf{x}, t_{\mathrm{ref}}, \tau)\, d\tau \tag{1}$$

(*Hall et al.*, 2002), where τ denotes the age of the water. $C^0(t)$ is the concentration history of the property in surface waters in the mixed layer. For upper water masses, we assume that $C^0(t)$ for CFCs and SF_6 is in solubility equilibrium with the atmosphere. For deeper, denser waters, the saturation decreases gradually to 80%. A detailed list of the saturation used for each density layer is given in the Supporting Information, Table A1. In *Steinfeldt et al.* (2009), the minimum saturation was chosen lower, i. e. 65%. However, CFC concentrations measured close to the formation region of NADW tend to be larger than 65% of the surface saturation (see Fig. B1), so the value for the minimum CFC saturation has been enlarged for all dense water data. According to *Steinfeldt et al.* (2009), the difference in the inferred C_{ant} concentrations is about half the saturation difference, i. e. a saturation difference of 20% leads to a C_{ant} difference of about 10%. For C_{ant}, we use a time independent carbon disequilibrium as in *Waugh et al.* (2006) and *Steinfeldt et al.* (2009). $C_{ant}(t_{\mathrm{ref}})$, is calculated as the difference between the carbon concentration at time t_{ref} and the preindustrial time (year 1800). If the carbon disequilibrium remains constant, it cancels out when calculating this difference. At the beginning of the industrial period, atmospheric CO_2 is increasing by about 1 ppm per decade. This means, an earlier or later start time for the beginning of the industrial period compared to 1800 would change the inferred C_{ant} concentration by about $0.6\,\mu\mathrm{mol\,kg}^{-1}$ per decade.

Eq.(1) will be used to infer concentrations of anthropogenic carbon ($C_{ant}(\mathbf{x}, t)$) from the TTD functions $\mathcal{G}(\mathbf{x}, t, \tau)$. On the other hand, Eq.(1) allows to infer the parameters of the TTD, such that $C(\mathbf{x}, t)$ are observed tracer concentrations. To do so, a certain functional form of the TTD has to be assumed. Here, we apply an inverse Gaussian function as approximation for the "real" TTD, as has been done in other studies (e. g. *Hall et al.* (2002); *Waugh et al.* (2006); *Steinfeldt et al.* (2009)). This function only depends on two parameters: the mean age (mean value of τ) Γ (first moment associated with the advective tracer transfer) and the width Δ (second moment, which is related to the dispersion or mixing on all relevant scales, including

recirculation and admixtures or entrainment of older water):

$$\mathcal{G}(\tau, \Gamma, \Delta) = \sqrt{\frac{\Gamma^3}{4\pi\Delta^2\tau^3}} \exp\left(\frac{-\Gamma(\tau - \Gamma)^2}{4\Delta^2\tau}\right). \tag{2}$$

215 In order to derive both parameters (Δ and Γ), simultaneous measurements of different anthropogenic tracers are needed (*Hall et al.*, 2002; *Steinfeldt et al.*, 2009; *Smith et al.*, 2011). As these are sparse, a fixed ratio of Δ/Γ is often used. This ratio is a measure for the importance of mixing (higher Δ/Γ values imply stronger mixing). *Waugh et al.* (2004) inferred a ratio of $\Delta/\Gamma = 1$ from tracer observations in the subpolar North Atlantic.

In an ideal case, if $\mathcal{G}$ would be the "real" TTD, the mean age Γ should be independent of the tracer from which it is
220 inferred. Eq.(1) then holds for CFC-12, CFC-11, SF_6 and any other tracer taken from the same water sample with identical TTD parameters. In reality, if Eq. 1 holds for one tracer (e. g CFC-12) with the regional Δ/Γ value, applying Eq. 1 with the same parameters of $\mathcal{G}$ to another tracer (e. g. CFC-11) may result in deviations of the order of a few % to the observed CFC-11 concentration. In this study, we use preferably CFC-12 derived ages, only when CFC-12 is not available, we use CFC-11. The number of the considered age data points is given in Table 1. CFC-12 and CFC-11 are the most commonly measured tracers
225 (Table 2). The advantage of CFC-12 is that it has increased in the atmosphere prior to CFC-11 and, for the recent years, shows a smaller decline (Fig. C1). For young waters, this decline leads to relatively large errors (from measurement uncertainties and an unknown mixed layer saturation) of the age and for the inferred anthropogenic carbon (*Tanhua et al.*, 2008). Thus, for data after 2005 in the upper layers ($0 < \sigma_\theta < 27.6\,\mathrm{kg\,m^{-3}}$) with young water (central and intermediate waters) and relatively high SF_6 concentrations, we use the SF_6 based age estimate, if available. If CFC-12 is measured simultaneously, it is used for the
230 calculation of the Δ/Γ ratio. In the subpolar Atlantic north of $45°$N, the density range for using the SF_6 age is expanded into the Labrador Sea Water, as this water mass there has also relatively young ages.

Steinfeldt et al. (2009) used pointwise TTDs with Δ/Γ ratios of 0.5, 1, or 2 for the subpolar to tropical Atlantic based on simultaneous observations of CFC-12/tritium and CFC-12/CFC-113. Here, we also make use of simultaneous measurements of CFC-12 and SF_6 to infer the Δ/Γ ratio and also rounded it to the quantized values of 0.5, 1, or 2. Note that SF_6 is not used
235 at all in the deep and bottom waters, as the concentrations could still be enlarged from the remnants of artificial tracer release experiments in the 1990s in the Nordic Seas (*Watson et al.*, 1999; *Tanhua et al.*, 2005) and Brazil Basin (*Polzin et al.*, 1997). Tritium is only used north of $45°$N. This excludes southern sources with lower surface tritium values. Including those would imply a spatial dependence of C^0 in Eq.(1), which is not applied here.

As in *Steinfeldt et al.* (2009), the inferred Δ/Γ ratios are gridded for each isopycnal layer in the same way as the other data
240 (see section 2.1). Due to the limited amount of tritium, CFC-113 and SF_6 observations compared to CFC-12, the data from all three decades are combined and any temporal change of the Δ/Γ ratio is not accounted for. Remaining data gaps of the gridded fields are filled with the standard value of $\Delta/\Gamma = 1$. The distribution of the resulting Δ/Γ ratios is shown in Fig. 3 a and b for the western and eastern basin of the Atlantic. We find high ratios close to the maximum value of 2 at the surface and in the newly formed AAIW, NADW (LSW, ISOW, DSOW) and AABW. For the latter, the precursor water masses WSBW
245 and WSDW directly North of Antarctica have a Δ/Γ ratio of about unity. Only the subtropical mode waters have Δ/Γ ratios
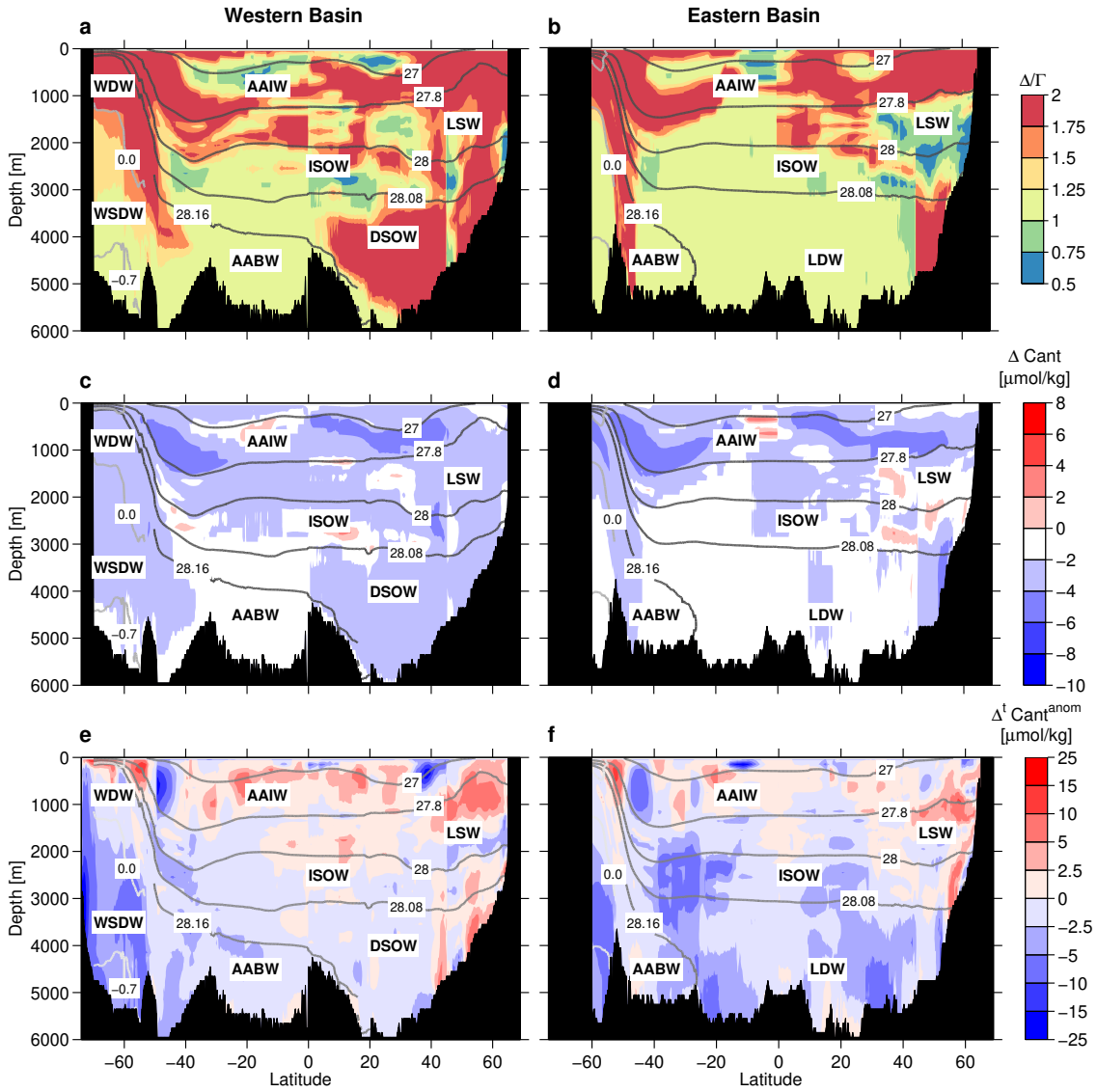
Figure 3. a–b: Zonal mean sections showing the Δ/Γ ratio inferred from simultaneous observations of different tracers. c–d: Difference in zonal mean C_{ant} concentrations calculated from a variable Δ/Γ ratio and from the constant ratio of $\Delta/\Gamma = 1$. The C_{ant} fields are based on tracer data from the whole period (1982–2021), the reference year is 2020. e–f: Zonal mean sections of $\Delta_t C_{ant}^{anom}$ for a variable Δ/Γ ratio (C_{ant} calculated for 2010 with data around 2010 minus C_{ant} calculated for 2010 based on tracer data around 1990, i. e. $C_{ant}^{2010} - C_{ant}^{1990 \to 2010}$). Contour lines are shown as in Fig. 2. For details see text.

below 1 near their formation region. Further downstream, the Δ/Γ ratio of the intermediate, deep and bottom waters decreases towards unity and even below, especially for LSW in the northeastern Atlantic.

Table 3. Hemispheric and total Atlantic C_{ant} inventories referenced to 2010 for thee different methods: the standard TTD method (as used e. g. in *Waugh et al.* (2006)), a variable Δ/Γ ratio (as used in *Steinfeldt et al.* (2009), and the modified TTD method with both a variable Δ/Γ ratio and an explicit dilution factor f.

| | Standard | Var. Δ/Γ | Var. Δ/Γ and dil. f |
	Cant [Pg C]	Cant [Pg C]	Cant [Pg C]
North	38.4	37.3	36.6
South	36.0	34.9	33.2
Total	74.4	72.2	69.9

The difference between the C_{ant} concentrations based on the variable Δ/Γ ratio and the case that $\Delta/\Gamma = 1$ is depicted in Fig. 3 c and d (here, the climatological C_{ant} fields referenced to 2010 are used). In general, $\Delta/\Gamma > 1$ leads to smaller,

250 and $\Delta/\Gamma < 1$ to larger values of the inferred C_{ant}, as has also been found in *He et al.* (2018). The areas with the $\Delta/\Gamma > 1$ dominate, but the basinwide reduction of the C_{ant} inventory due to the variable Δ/Γ ratio is only of the order of 1 Pg C (Table 3) both for the North and the South Atlantic. In the study by *He et al.* (2018), the best agreement between the directly modeled global C_{ant} inventory and C_{ant} inferred from the TTD method is for a mean Δ/Γ ratio of 1.2, which is similar to our results for the Atlantic.

255 One advantage of the TTD method is that it allows for the choice of the reference year t_{ref} in Eq.(1). This makes it possible to group observations from several years to calculate C_{ant} for a common reference year, as it has been done here for CFC/SF$_6$ data from 1982–1994, 1995–2005, 2006–2013, 2014–2021 and using all data from 1982–2021. By varying t_{ref} in Eq. (1), the TTD method also allows to make predictions for future tracer concentrations. If the TTD parameters have been determined from a tracer observation at time t_{obs}, t_{ref} can be shifted into the future and the concentration of any tracer can be inferred

260 from Eq.(1) for this future time t_{ref}. The assumption underlying this prediction is that the TTD function $\mathcal{G}$ remains the same, $\mathcal{G}(\mathbf{x}, t_{\mathrm{obs}}, \tau) = \mathcal{G}(\mathbf{x}, t_{\mathrm{ref}}, \tau)$, i. e. the ocean circulation and ventilation does not change. The increase of C_{ant} in this case is thus only due to the rising atmospheric CO_2. In particular, we use the tracer data from around 1990 (1982–1994) to predict C_{ant} for the reference year 2020. These predicted C_{ant} values are denoted by $C_{\mathrm{ant}}^{1990 \rightarrow 2020}$. This prediction can be compared with the case where C_{ant} is inferred from data around the reference year. C_{ant}^{2020}, e. g. means C_{ant} calculated from data between

265 2013–2021 and referenced to the year 2020. The difference $C_{\mathrm{ant}}^{2020} - C_{\mathrm{ant}}^{1990 \rightarrow 2020}$ can be interpreted as anomaly of the C_{ant} increase (or accumulation) between 1990 and 2020 due to changes in the oceanic circulation/ventilation (i. e. in the TTDs) and will thus be denoted $\Delta_{\mathrm{t}} C_{\mathrm{ant}}^{\mathrm{anom}}$, as in *Gruber et al.* (2019). These anomalies can also be inferred for the other decadal C_{ant} increase rates, i. e. $C_{\mathrm{ant}}^{2000} - C_{\mathrm{ant}}^{1990 \rightarrow 2000}$ and $C_{\mathrm{ant}}^{2010} - C_{\mathrm{ant}}^{2000 \rightarrow 2010}$.

Fig. 3 e–f show the distribution of $\Delta_{\mathrm{t}} C_{\mathrm{ant}}^{\mathrm{anom}}$ for the western and eastern basin for the case $C_{\mathrm{ant}}^{2020} - C_{\mathrm{ant}}^{1990 \rightarrow 2020}$. The C_{ant}

270 anomalies will be discussed in detail in section 3.3.2. Here, we only want to point out that in some cases large anomalies are found in the formation region of a water mass, e. g. for LSW and AAIW in the western Atlantic, and, less pronounced, also in the eastern basin. Also the WSDW and AABW exhibit large negative anomalies. Further downstream, in the equatorial region,

the anomalies within LSW and AAIW are slightly smaller. This is to be expected, as away from the source region waters from different vintages with different C_{ant} anomalies mix. However, we also find strongly negative values of $\Delta_t C_{ant}^{anom}$ in the LDW in the eastern Atlantic, which is the oldest water mass and not in the direct export path way of AABW or DSOW. In these old waters, a pronounced C_{ant} anomaly should only occur for a pronounced longtime change in the ocean circulation/ventilation. But even then, the C_{ant} accumulation anomaly should be smaller than in the regions with high C_{ant} concentrations like the water mass formation regions. Older waters contain a notable fraction with ages larger than 200 yr (see the example in Table D1), i. e. C_{ant} free waters, which cannot contribute to the C_{ant} anomaly. We thus consider the strongly negative $\Delta_t C_{ant}^{anom}$ values in LDW as an artefact of the TTD parameterization in the form of a single inverse Gaussian function. In the next section we show how a modification of the TTD parameterization by including an additional dilution of young with old waters helps to overcome this artefact.

2.3.2 The modified TTD method with dilution

Steinfeldt and Rhein (2004) presented the foundation of the TTD method applied here by focusing on the Deep Western Boundary Current (DWBC) of the tropical Atlantic and investigating the NADW therein as a mixture of young and old water contributions. We will apply the same principle here, but in contrast to the previous study extend this approach to the entire Atlantic Ocean.

$$\mathcal{G} = f \cdot \mathcal{G}_{young} + (1 - f) \cdot \mathcal{G}_{old} \tag{3}$$

$\mathcal{G}_{old}$ is assumed to not contain CFCs and also no C_{ant}, thus we do not need to consider it here. The additional parameter f describes the fraction of younger water, and $1 - f$ the "dilution" with old water. Eq. 1 then becomes:

$$C(\mathbf{x}, t_{ref}) = \int_0^\infty C^0(t_{ref} - \tau) \cdot f \cdot \mathcal{G}_{young}(\mathbf{x}, t_{ref}, \tau) \, d\tau. \tag{4}$$

The dilution of younger water with an old component can be interpreted as follows: In the North Atlantic, the younger water can be interpreted as NADW, and the old water as admixtures of AABW or recirculated NADW. In the South Atlantic, young waters are AABW and AAIW, and the old water originates from NADW. We also introduce an age threshold below which the dilution case is excluded. This is chosen as $\Gamma_{young} = 100$ yr. Mean ages younger than 100 yr only occur in and close to water mass formation regions, where a dilution with waters free of anthropogeic tracers is unlikely. Thus it is guaranteed that for these relatively young waters e. g. in the vicinity of water mass formation regions where the temporal variability might be high, only the no dilution case is applied.

In order to determine f, *Steinfeldt and Rhein* (2004) used assumptions that are only valid in the DWBC. Here, we want to apply the dilution at any region, especially for old water like the LDW, far away from the DWBC. The method to determine the fraction f is as follows: For $f = 1$, we calculate C_{ant} as described above with the Δ/Γ ratios determined from simultaneous observations of different transient tracers. In addition, we infer C_{ant} for values of f of 0.75, 0.5, and 0.25 with $\Delta/\Gamma = 1$. These quantized values are chosen to limit the computational effort and obtain marked differences between the derived C_{ant} concentrations. From the four sets of TTD parameters four different C_{ant} values are inferred.
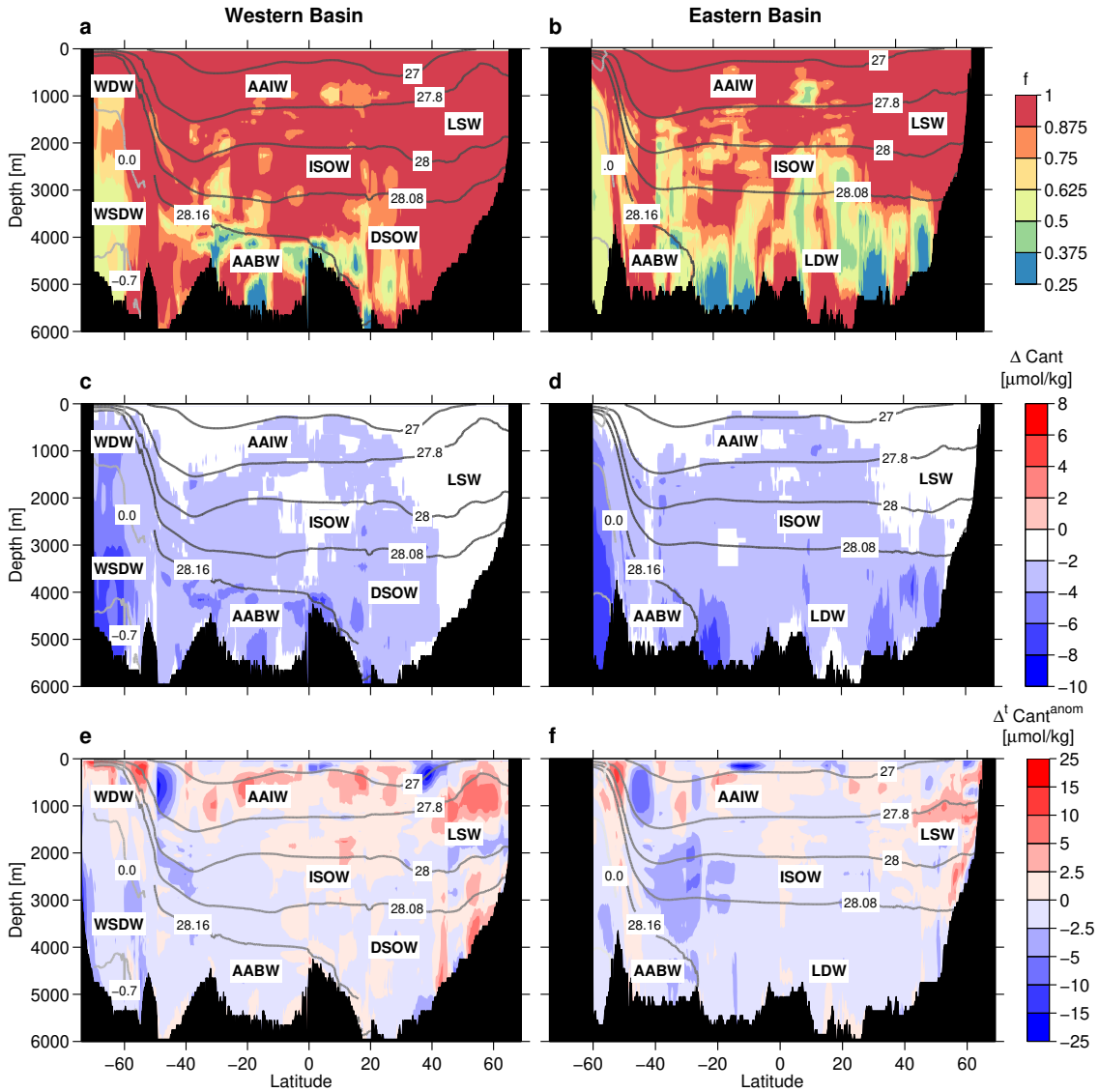
Figure 4. a–d: Zonal mean sections showing the fraction f of young, C_{ant} bearing water. c–d: Difference in zonal mean C_{ant} concentrations between the calculated from a variable Δ/Γ ratio and no dilution and a variable Δ/Γ ratio with dilution. The C_{ant} fields are based on tracer data from the whole period (1982–2021), and the reference year is 2020. e–f: Zonal mean sections of $\Delta_t C_{ant}^{anom}$ for a variable Δ/Γ ratio (C_{ant} calculated for 2010 with data around 2010 minus C_{ant} calculated for 2010 based on tracer data around 1990, i. e. $C_{ant}^{2010} - C_{ant}^{1990 \to 2010}$). Contour lines are shown as in Fig. 2. For details see text.

305   At each grid point, from these four TTD parameterizations that one is chosen which minimizes the C_{ant} differences between the climatology and the decadal values, i. e.:

$$\min(C_{ant}(1982-1994)^{1990} - C_{ant}(clim)^{1990})^2 + (C_{ant}(1995-2005)^{2000} - C_{ant}(clim)^{2000})^2 +$$

$(C_{ant}(2006-2013)^{2010} - C_{ant}(clim)^{2010})^2 + (C_{ant}(2014-2021)^{2020} - C_{ant}(clim)^{2020})^2$ where, e. g., $C_{ant}(1982-1994)^{1990}$ means C_{ant} referenced to 1990 inferred form the decadal data from 1982–1994, and $C_{ant}(clim)^{1990}$ means the climatological

310   C_{ant} value referenced to 1990. An example for the influence of varying the TTD parameters (Δ/Γ ratio, fraction f) on the shape of the TTD is given in Fig. D1.

The inferred fractions f are shown in Fig. 4a–b for the western and eastern basin. Close to the water mass formation regions, e. g. the subpolar North Atlantic, the waters are too young to allow for a dilution, so f is set to 1 there. The only exception is the WSDW, which has a dilution factor of about 0.5 adjacent to its formation region (the formation region itself at the Antarctic

315   shelf is not considered here). A strong dilution with old waters (low f) is mainly found in the deep and bottom waters (AABW, LDW and DSOW south of $30°N$). In these regions, the inferred C_{ant} concentrations are remarkably smaller than for the case without dilution (see Fig. 4c–d) by upto $10\,\mu mol\,kg^{-1}$. In general, the regions with $f < 1$ always show a reduction in C_{ant}. For the North Atlantic, where the regions with $f = 1$ dominate, the basinwide C_{ant} inventory is only reduced by 0.7 Pg C compared to the TTDs without dilution. For the South Atlantic, this reduction is larger, 1.7 Pg C (Table 3).

320   The introduction of the dilution f does not only lead to smaller C_{ant} concentrations, but also to a reduction of the amount of the C_{ant} accumulation anomalies $\Delta_t C_{ant}^{anom}$. A comparison between Fig. 3 e–f and 4 e–f shows that $\Delta_t C_{ant}^{anom}$ becomes less negative especially in the waters of Antarctic origin (WSDW, AABW and LDW), where $f < 1$. On the other hand, the positive C_{ant} anomalies in the NADW, especially the LSW, in the western tropical Atlantic hardly change, i. e. they are less dependent from the parameterization of the TTDs. In section 3.3.2 we will relate these C_{ant} accumulation anomalies with

325   observed changes in ocean ventilation. As the spuriously negative values of $\Delta_t C_{ant}^{anom}$ in the old deep waters are reduced by taking into account the dilution of young with old water, we will use the modified TTDs with dilution to compute the Atlantic C_{ant} inventories. Another advantage of this TTD parameterization is that it reduces the relatively high C_{ant} concentrations in the Southern Ocean that results from the standard TTD method compared to other C_{ant} calculation techniques (*Waugh et al.*, 2006; *Vázquez-Rodríguez et al.*, 2009; *Khatiwala et al.*, 2013).

330   The strongly negative C_{ant} accumulation anomalies, when using the standard TTDs, indicate that the water in 2020 is older than in 1990, thus C_{ant} calculated from the age in 1990 with reference year 2020 is larger than C_{ant} derived from the age in 2020. Fig. 5 shows, that the CFC-increase rate for a steady state ocean (calculated from Eq.(1)) CFC-12 in the year 2000 is smaller for smaller fractions f. If an observed CFC increase over time (around the year 2000) lags the expected value from Fig. 5, the water becomes older, and vice versa. Thus the choice of the dilution factor f influences age changes inferred from

335   observed temporal changes of the CFC-12 concentration. As a consequence, the magnitude of the C_{ant} anomaly $\Delta_t C_{ant}^{anom}$ also differs between different TTD parameterisations.

2.3.3   Error estimation

The error of C_{ant} is calculated in a similar way as in *Steinfeldt et al.* (2009). The contributions of the interpolation/gridding error (3 %), the C_{ant} disequilibrium (possible undersaturation) (20 %), the CFC disequilibrium (5.5 %, including errors in the

340   CFC measurements) are treated the same. The C_{ant} uncertainty in very old waters of $2.0\,\mu mol\,kg^{-1}$ (*Steinfeldt et al.*, 2009) is considered as minimum error everywhere. If the CFC-12 concentration is below the typical detection limit of $0.005\,pmol\,kg^{-1}$,
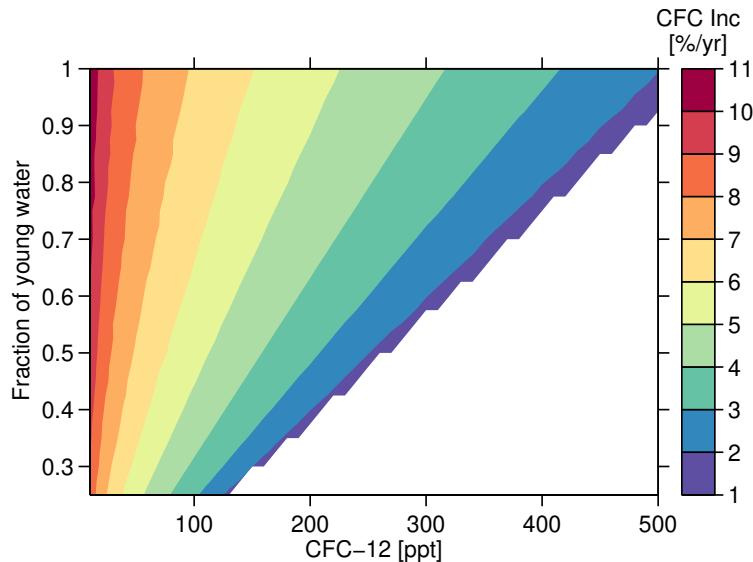
Figure 5. Expected increase rate (Inc) per year of CFC-12 for a concentration observed in year 2000 as a function of the observed CFC-12 concentration itself and the fraction of young water. The increase is calculated from the TTDs inferred from the CFC-12 concentration in the year 2000, assuming a stedy state ocean. High CFC-12 concentrations are incompatible with low fractions of young water, this area is left blank. For details see text.

the C_{ant} concentration is set to zero. The error due to the TTD parameterization as an Inverse Gaussian function compared to the "real" TTD is the maximum of the 20% given in *Steinfeldt et al.* (2009) and the difference in C_{ant} calculated with the standard TTD method and the case with dilution. In the model study by *He et al.* (2018), the error arising from a change of the

345   C_{ant} disequilibrium is relatively low (less than 10% for all ocean regions), so our assumption might be an overestimation.

All these errors apply to the C_{ant} value at each data point. For the gridded fields, the statistical errors reduce according to the degrees of freedom, whereas the systematic errors remain unchanged. The errors due to the shape of the TTD and the unknown C_{ant} disequilibrium are assumed to be similar (or systematic) within one water mass, but may vary between water masses. As there are about four different water mass classes (Central and Intermediate Water, LSW, Overflow Waters, and AABW), these

350   errors are divided by $\sqrt{4} = 2$ when the error for the total inventory is considered. The C_{ant} error of $2.0\,\mu mol\,kg^{-1}$ at low CFC concentrations can be regarded as cruise dependent. Most grid points are influenced by at least two cruises (e. g. a zonal and a meridional section). Thus the error of $2.0\,\mu mol\,kg^{-1}$ is divided by $\sqrt{2}$ for each grid point and by $\sqrt{n}$, for the whole inventory, where n denotes the number of cruises from which the gridded C_{ant} data is inferred.

For inventory differences of C_{ant} between times t_1 and t_2, the errors due to a change in C_{ant} and CFC disequilibria and the

355   errors due to uncertainties in the TTD shape only have to be applied to the portion of C_{ant} that is added between t_1 and t_2. For the water formed prior to time t_1, which is still present at time t_2, these systematic errors mainly cancel out (*Steinfeldt et al.*, 2009).

Table 4. Atlantic C_{ant} inventories in Pg C for reference years 1990, 2000, 2010 and 2020 based on all tracer data and on tracer data from the decade centered around the reference year only.

	1990	2000	2010	2020
	all data	all data	all data	all data
North	21.9 ± 3.4	26.1 ± 3.9	31.0 ± 4.8	36.6 ± 5.7
South	20.0 ± 3.3	23.7 ± 3.6	28.1 ± 4.7	33.2 ± 5.5
Total	41.9 ± 6.7	49.8 ± 7.4	59.1 ± 9.5	69.9 ± 11.2
	data from	data from	data from	data from
	1982–1994	1995–2005	2006–2013	2014–2021
North	21.8 ± 3.5	26.1 ± 3.9	31.1 ± 4.8	36.7 ± 5.6
South	21.2 ± 3.8	23.3 ± 3.5	26.9 ± 4.5	31.6 ± 5.2
Total	43.0 ± 7.3	49.4 ± 7.4	58.0 ± 9.3	68.2 ± 10.8

When comparing the predicted C_{ant} values for time t_2 based on observations at t_1 with the C_{ant} values based directly on observations at t_2, the error due to a change in the C_{ant} disequilibrium is neglected. The reason is that here we are interested in the effect of a change in age on the C_{ant} concentrations and not in the effect of biogeochemical changes. Second, a change in the C_{ant} disequilibrium would effect the C_{ant} values for the prediction from observations at t_1 and from more recent observations at t_2 in a similar way.

3 Results and Discussion

3.1 Basin-wide C_{ant} distribution

The C_{ant} concentration and inventories of the Atlantic between $70°$S and $65°$N are computed for the reference years 1990, 2000, 2010 and 2020 from the decadal CFC/SF$_6$ data. In addition, we use all data to calculate a quasi climatological distribution of the Atlantic C_{ant} inventories for the same reference years. All inventories and their uncertainties are listed in Table 4. The Atlantic inventory of about $58.0 \pm 9.3\,\mathrm{Pg\,C}$ in 2010 makes up $37 \pm 9\,\%$ of the global C_{ant} storage ($155\,\mathrm{Pg\,C}$, "best estimate" in *Khatiwala et al.* (2013)), whereas the fractional areal cover of the parts of the Atlantic considered here is only about 22 %.

The climatological column inventory obtained from the extended TTD method is shown in Fig. 6. A tongue of high C_{ant} column inventories stretches southward from the C_{ant} maximum in the northwestern Atlantic towards the equator. This reflects the southward propagation of NADW, mainly within the DWBC (*Rhein et al.*, 2015). NADW is relatively high in C_{ant} compared to the deep water masses of southern origin.

The zonal mean sections for the eastern and western basin of the Atlantic shown in Fig. 7 highlight the vertical C_{ant} distribution and the contributions of the different water masses to the column inventory. C_{ant} concentrations are high at the surface
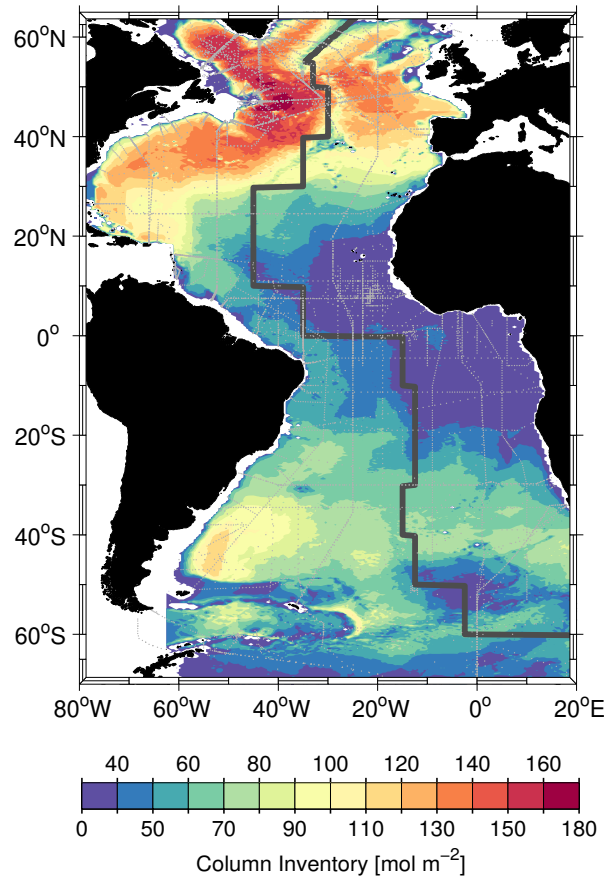
Figure 6. Map of the climatological C_{ant} column inventory referenced to 2020 based on all tracer data between 1982 and 2021. The thick line following the Mid-Atlantic Ridge indicates the boundary between eastern and western basin. Dots indicate the locations of tracer samples used for the C_{ant} calculation.

and in the central waters formed in the subtropical gyres. The maximum is found at the surface in the tropical/subtropical zone, where SST is highest. The reason is that the C_{ant} equilibrium concentration increases with temperature and alkalinity. Especially the subtropical gyres show high values of salinity and also alkalinity (*Lee et al.*, 2006). The AAIW layer below
380   forms a kind of transition zone between the C_{ant}-rich mode waters above and the C_{ant}-poor old deep waters below.

The most striking feature in the deep waters are the elevated C_{ant} concentrations in the North Atlantic (Fig. 7). They are highest in the western basin in the LSW layer, as this water mass is directly formed there (see section 2.2). The spreading time for DSOW from its origin in the Nordic Seas towards the Labrador Sea is about $5\,\mathrm{yr}$ (*Rhein et al.*, 2015), resulting in lower C_{ant} concentrations. The NADW component with the lowest C_{ant} values is the ISOW, as this water mass has the longest travel
385   time into the western Atlantic via the Charlie-Gibbs Fracture Zone (*Smethie and Swift*, 1989). The northeastern Atlantic does in general exhibit smaller C_{ant} values in the deep waters. The LSW is also present there, but with lower concentrations due
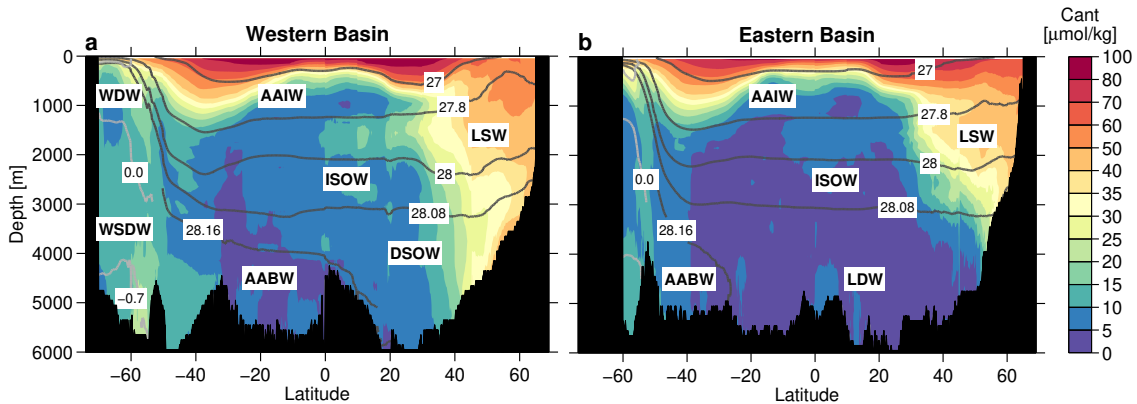
Figure 7. Zonal mean sections of C_{ant} referenced to 2020 based on all tracer data between 1982 and 2021. a: western basin, b: eastern basin. Contour lines are shown as in Fig. 2.

to the spreading time of around 5 yr from the formation region in the Labrador Sea towards the European continent (*Sy et al.*, 1997; *Yashayaev et al.*, 2007). The ISOW in the eastern basin does not reach the bottom of the deep basin, and the DSOW is not able to cross the Mid-Atlantic Ridge towards the east in the North Atlantic, so the deepest waters in the eastern basin (LDW) are low in C_{ant}. The southward spreading of NADW mainly in the DWBC leads to a tongue of enhanced C_{ant} concentrations in the western basin which reaches south of the equator. The slightly enhanced concentrations in the LSW and AABW in the eastern equatorial Atlantic are due to the import of deep water from the western basin (*Rhein and Stramma*, 2005).

Also in the deep South Atlantic C_{ant} in deep waters decrease from west to east. The higher C_{ant} concentrations in the west are due to the spreading of AABW, which propagates from the Weddell Sea northward into the deep basins of the western Atlantic (*Orsi et al.*, 1999). Another AABW branch continues eastward near 60°S. This branch can be seen in the enhanced C_{ant} values in Fig. 7a. It is also identified in the Prime Meridian Section in *Huhn et al.* (2013) by the deep CFC-12 maximum. The C_{ant} concentrations in the AABW core are considerable smaller compared to NADW. Through the entrainment of old WDW (see section 2.2), the transient tracer signal of AABW gets diluted, which explains the smaller C_{ant} values.

To compare our results directly with other methods, Fig. 8 shows the C_{ant} distributions in the western and eastern Atlantic from *Sabine et al.* (2004) (ΔC^* method) and *Khatiwala et al.* (2013) (Green's function method (GF)). Here, all C_{ant} values are referenced to 1994. For our TTD derived C_{ant} distribution we only use data from the first two decades (1982–2005) to have a similar data basis as the other studies. In the upper waters, the high C_{ant} concentrations in the North East Atlantic Central water betwen 40°N and 60°N from the ΔC^* method stick out. Otherwise, all methods yield similar results. This is different for the deep waters. There, the pattern of the C_{ant} distribution differs. The high C_{ant} concentrations in the cores of DSOW (between 40°N and 60°N) and AABW (around 60°S) in the western basin can only be found in the TTD method. For the ΔC^* method, C_{ant} in the deep waters (ISOW, DSOW, LDW and AABW) is in general low and sometimes even has (unrealistic) negative values. For LSW, however, the results from the ΔC^* and TTD method agree quite well. For this water mass, the GF
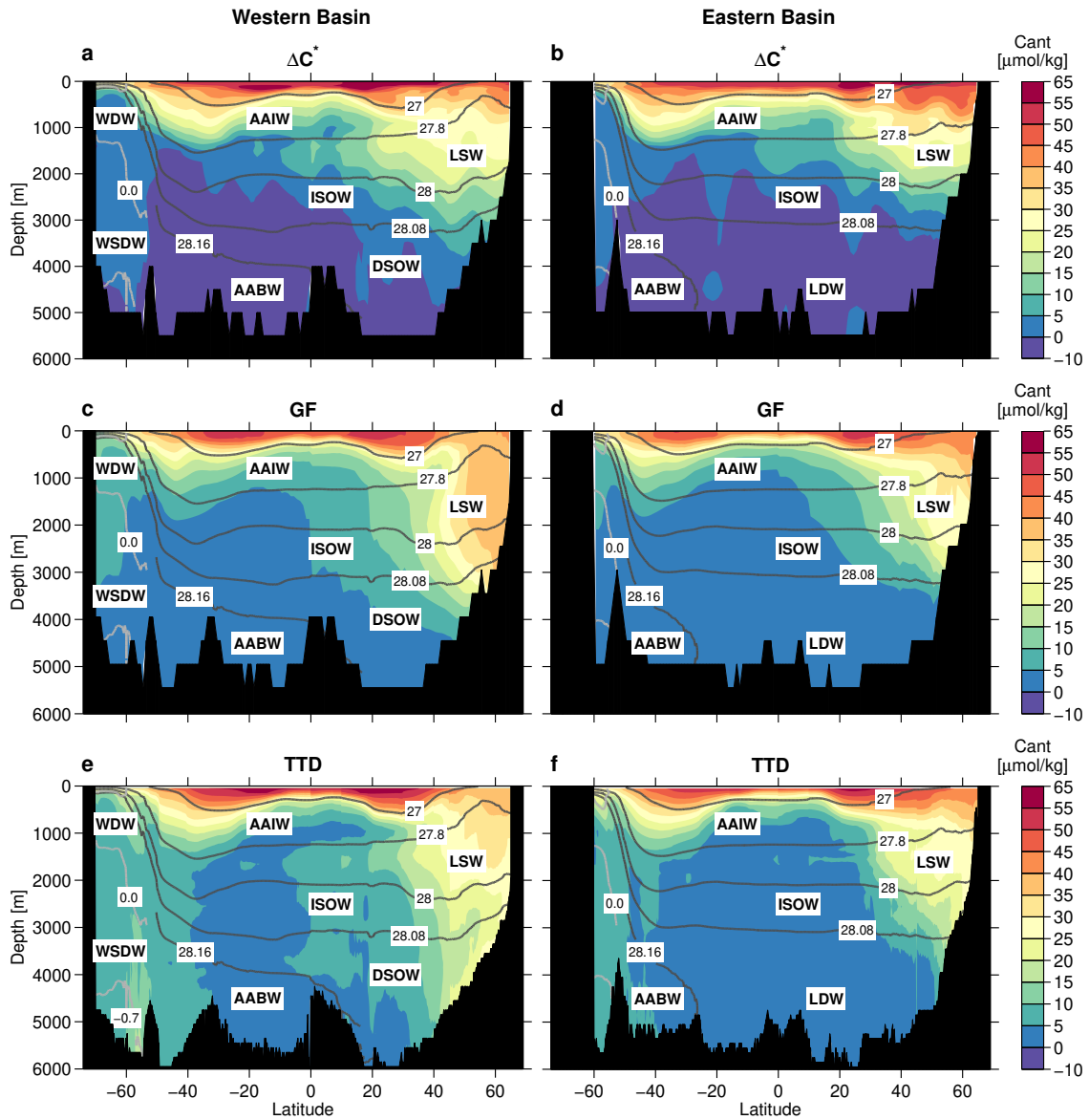
Figure 8. Zonal mean sections of C_{ant} referenced to 1994 from a–b: the ΔC^* method (*Sabine et al.*, 2004), c–d: the GF method (*Khatiwala et al.*, 2013), e–f: our TTD method. Contour lines are shown as in Fig. 2.

method yields the highest concentration, especially in the western basin. Regarding the deeper water masses below the LSW, the results from the GF method are in between the ΔC^* and TTD values.

410   Overall, the improved TTD method used here leads to C_{ant} distributions that are compatible with the spreading of the water masses. The low C_{ant} values from the ΔC^* and GF method in the recently formed DSOW and AABW are an unlikely scenario,
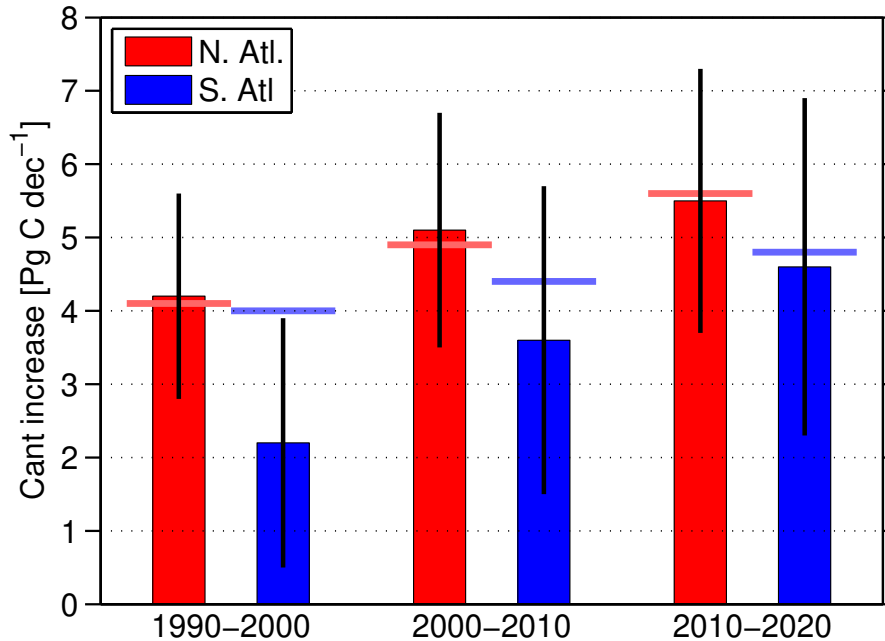
Figure 9. Decadal changes (1990–2000, 2000–2010 and 2010–2020) of the C_{ant} inventories for the North (N. Atl.) and South (S. Atl.) Atlantic. The vertical black lines indicate the uncertainties. The horizontal coloured lines show the inventory increase based on the C_{ant} inventory from the beginning of the decadal period (1990, 2000 and 2010 respectively) and a steady state ocean circulation.

as these water masses contain considerable amounts of CFCs (*Smethie et al.*, 2000; *van Heuven et al.*, 2011; *Huhn et al.*, 2013), which have been in the atmosphere for a shorter time than C_{ant}.

3.1.1 C_{ant} increase 1990–2020

415   The decadal changes in C_{ant} inventories ($\Delta_t C_{ant}$) are depicted in Fig. 9 and given in Table 5 together with results from other studies. Our results show a continuous increase of $\Delta_t C_{ant}$ over the three decades for both hemispheres. The North Atlantic does show the higher C_{ant} storage compared to the southern part. This difference is most pronounced for the first decade from 1990 to 2000.

   The results from the other studies often show larger values of $\Delta_t C_{ant}$ in the South and smaller ones in the North Atlantic.
420   This is especially the case for the 1990–2000 period in *Woosley et al.* (2016) (1.9 ± 0.4 Pg C compared to 4.2 ± 1.4 Pg C in our study). The results in *Woosley et al.* (2016) are based on the eMLR method, and the values for the for period 1990–2000 are adopted from *Wanninkhof et al.* (2010). There, the C_{ant} change over the whole Atlantic is inferred from only one cruise which, in the North Atlantic, is located in the eastern basin and hence does not cover the deep water formation areas in the Irminger and Labrador Sea. This may introduce a bias in the results compared to our study. For the second period from 2000–
425   2010, *Woosley et al.* (2016) use four cruises, also a small number compared to the amount of cruises/data used in this study.

Table 5. Decadal changes in Atlantic C_{ant} inventories ($\Delta_t C_{ant}$, in Pg C). The inventory differences are obtained from the "decadal data only" inventories listed in Table 3. They are compared with the values given in *Woosley et al.* (2016) (based on the eMLR method, the C_{ant} increase from 1990 to 2000 in *Woosley et al.* (2016) is adopted from *Wanninkhof et al.* (2010)), and *Müller et al.* (2023) (eMLR(C^* method), the increase there is calculated for the periods 1994–2004 and 2004–2014).

	this study	*Woosley et al.* (2016)	*Müller et al.* (2023)
1990–2000			
North	4.2 ± 1.4	1.9 ± 0.4	4.8 ± 0.2^a
South	2.2 ± 1.7	3.2 ± 0.7	3.9 ± 0.5^a
Total	6.4 ± 2.8	5.1 ± 1.0	8.7 ± 0.7^a
2000–2010			
North	5.1 ± 1.6	4.4 ± 0.9	3.9 ± 0.4^b
South	3.6 ± 2.1	3.7 ± 0.8	5.4 ± 0.6^b
Total	8.6 ± 3.4	8.1 ± 1.6	9.3 ± 1.0^b
2010–2020			
North	5.5 ± 1.8		
South	4.6 ± 2.3		
Total	10.2 ± 3.5		

[a] value for the period 1994–2004

[b] value for the period 2004–2014

Nevertheless, the agreement for the second decade with *Woosley et al.* (2016) is good 5.1 ± 1.6 Pg C vs. 4.4 ± 0.9 Pg C). For the South Atlantic, the values in *Woosley et al.* (2016) are higher than ours, especially for the period 1990–2000, but still agree within the error range.

By applying the eMLR(C^*) method to inorganic carbon observations obtained from the previous GLODAPv2 version, *Müller et al.* (2023) infer the increase in the Atlantic C_{ant} inventory for the periods 1994–2004 and 2004–2014. Unfortunately, these periods are shifted compared to ours by four years, which hampers a direct comparison with our results. Due to the four year shift, the values in *Müller et al.* (2023) should be larger by about 8% (see section 3.3.2) when the ocean circulation would be in steady state. The most striking difference to our results is the decrease of $\Delta_t C_{ant}$ in the North Atlantic between the periods 1994–2004 and 2004–2014. As in *Woosley et al.* (2016), also the study by *Müller et al.* (2023) yields higher C_{ant} storage rates in the South Atlantic compared to our results.

3.2 Local C_{ant} changes

We will now discuss the decadal C_{ant} changes between 1990 and 2020 in different regions/water masses of the Atlantic. Fig. 10 shows the mean annual storage rates for the respective decades between 1990 and 2020 and the total time period 1990–2020 over the whole water column (Fig. 10a, c, e) and the deep and bottom water layers only (Fig. 10b, d, f), which comprise the

$\sigma_{1.5}$ and σ_4 layers from table A1. Fig. E1 shows the same C_{ant} changes as Fig. 10, but expressed as relative numbers. In Fig. 11 the changes in C_{ant} concentrations in the western and eastern basin are depicted. The C_{ant} increases shown in Fig. 10 and Fig. 11 reveal similar patterns as the C_{ant} distribution in Fig. 6 and Fig. 7, i.e. the C_{ant} increase over time is high where the C_{ant} concentration is also high. The largest increase appears close to the surface and in the subtropical mode waters, also the NADW contributes significantly to the Atlantic C_{ant} storage. This becomes particularly evident when comparing the C_{ant} increase for the whole water column (Fig. 10a, c, e) with those for the deep and bottom waters only (Fig. 10b, d, and f): In the subpolar North Atlantic, where the deep water layer reaches close to the surface, the C_{ant} storage in deep and bottom waters alone is almost as large as for the total water column. The southward propagation of NADW in the western basin is reflected by a significant C_{ant} increase that extends to $10°S$ and is most pronounced in the LSW layer (Fig. 11a, c and e). In the eastern basin, any noticeable spatial C_{ant} increase of the younger NADW layer (LSW and ISOW) is limited to the region north of $30°N$.

The deep and bottom waters in the Atlantic that are not influenced by younger NADW mainly show insignificant C_{ant} changes. South of about $40°S$, the AABW exhibits a C_{ant} increase above the detection limit at least in some places These also contribute to the increase in the column inventory of the deep and bottom waters south of $40°S$ shown in Fig. 10f. The differences between the decadal C_{ant} storage rates will be discussed in more detail in section 3.3 on decadal variability.

3.2.1 Comparison of local C_{ant} changes from the modified TTD method with dilution with other publications

We now compare our inferred local C_{ant} changes in the Atlantic with other published results. For the subpolar North Atlantic, the area with the highest increase in C_{ant} column inventory, *Pérez et al.* (2010) find similar storage rates ($1.74\,\mathrm{mol\,m^2\,yr^{-1}}$ in the Irminger Sea and $1.88\,\mathrm{mol\,m^2\,yr^{-1}}$ in the Iceland basin) as shown in Fig. 10, but only from 1991 to 1997, where the North Atlantic Oscillation (NAO) was in a high phase. Afterwards, in the low NAO period between 1997 and 2006, their rate is less than a quarter of the previous value ($0.3 - 0.4\,\mathrm{mol\,m^2\,yr^{-1}}$). Also for the northeastern Atlantic, *Pérez et al.* (2010) yield lower storage rates ($0.72\,\mathrm{mol\,m^2\,yr^{-1}}$ for 1981–2006) compared to our analyses ($> 1.0\,\mathrm{mol\,m^2\,yr^{-1}}$, Fig. 8a, c, d). In contrast to *Pérez et al.* (2010), our results are averaged over a larger region and also a longer time period (a decade compared to six and nine years in *Pérez et al.* (2010) for the Irminger and Iceland basin), which may lead to a damping of sudden, regional changes in the C_{ant} storage. However, the low C_{ant} increase in *Pérez et al.* (2010) after 1997 also points to methodological differences between the φC_T^0 method used in *Pérez et al.* (2010) and the modified TTD method with dilution used here. One of these is that the φC_T^0 method takes into account changes in the ocean air-sea CO_2 disequilibrium over time. On the other hand, a comparison of Fig. 11a and 11c indicates that in the decade 2000–2010 the C_{ant} storage in the deeper part of the LSW is indeed very small (due to a reduction in the convection depth). The other water masses, however, i. e. the Overflow Waters and the waters above $1000\,\mathrm{m}$, do not show a decrease in the C_{ant} uptake, in agreement with the ongoing renewal of these water masses. Thus, the small increase of the C_{ant} column inventory after 1997 in *Pérez et al.* (2010) seems to be unrealistic. Directly within the Labrador Sea, *Raimondi et al.* (2021) find a mean storage rate of ($1.8\,\mathrm{mol\,m^2\,yr^{-1}}$ for the period 1986–2016. The largest rates occur at the end of the time series, and the smallest between 2005 and 2010. This is in good agreement with our indings (see Fig. 10a, c, and d, the western box between $50°N$ and $60°N$).

In the western South Atlantic the C_{ant} increase from our modified TTD method is similar to the results in *Ríos et al.* (2012) based on the φC_T^0. The C_{ant} storage is highest in the Central Water, decreases downward with a minimum in the lower part of the NADW and shows some patches of significant C_{ant} increase towards the AABW near the bottom south of $50°$S (Fig. 11c). In the Weddell gyre along the Prime Meridian, *van Heuven et al.* (2011) also find significant C_{ant} changes near the bottom. Applying the MLR method, they get an increase rate of $0.445\,\mu\text{mol kg}^{-1}$ per decade, whereas the trend of the directly observed carbon data is $1.15\,\mu\text{mol kg}^{-1}$ per decade. The latter compares well with our C_{ant} increase of about $1-2\,\mu\text{mol kg}^{-1}$ per decade, Fig. 11c. *van Heuven et al.* (2011) do not provide a full explanation for the discrepancy between the directly observed carbon increase and that derived from the MLR method. The comparison to our results supports their conclusion that the larger directly observed carbon trend could be probably ascribed primarily to the increase of C_{ant}, although the reason for the lower trend in the MLR results remains unexplained.

Müller et al. (2023) find the highest increase of the C_{ant} column inventory between 1994 and 2004 in the subtropical North Atlantic. The value of about $16\,\mu\text{mol m}^{-2}$ per decade is similar to our findings (Fig. 10), but our maximum in the subpolar western North Atlantic does not show up there. One reason could be, that the column inventory in *Müller et al.* (2023) does not take into account waters below $3000\,\text{m}$ depth, to avoid the imprint of errors from the eMLR(C*) method. This implies that the C_{ant} rich DSOW core In the western subpolar North Atlantic is missing in that study. For the second period (2004–2014) considered in *Müller et al.* (2023), the maximum of the increase of the C_{ant} column inventory is located in the western subtropical South Atlantic. The same holds for the C_{ant} increase estimated in *Gruber et al.* (2019) for the period 1994–2007, also based on the eMLR(C*) method. Our estimates of the C_{ant} column inventory always have their maximum in the North western Atlantic, either between $40°$ and $50°$N or between $50°$ and $60°$N (Fig. 11a, c, and d).

3.3 Decadal variability of C_{ant} storage

As mentioned above, the TTD technique in general allows to make predictions for C_{ant} concentrations based on older observations if one assumes a steady state ocean, i. e. the TTD $\mathcal{G}$ remains constant with time. In this case, the C_{ant} increase with time is solely due to the rising atmospheric CO_2. The TTD method thus allows to distinguish between the C_{ant} variability generated by changes in oceanic circulation (which implies a change of the TTD) and the expected C_{ant} increase with time resulting merely from the atmospheric CO_2 increase.

3.3.1 Evolution of C_{ant} for a steady state ocean

We will first consider the effect of the rising atmospheric CO_2 on the oceanic C_{ant} concentrations. If the mixed layer concentration of the tracer C^0 increases exponentially with time, $C^0(t+\Delta t) = C^0(t)\exp(\lambda\Delta t)$, then, following Eq. 1, the concentration of C in the ocean interior increases in the same way, $C(\mathbf{x}, t+\Delta t) = C(\mathbf{x}, t)\exp(\lambda\Delta t)$. *Steinfeldt et al.* (2009) applied an exponential fit of $C_{ant}^0(t)$ for the time 1850–2003 and yielded a mean growing rate of $1.69\,\%\,\text{yr}^{-1}$. Note that the increase rate of the equilibrium surface concentration $C_{ant}^0(t)$ is smaller by about $0.3\,\%\,\text{yr}^{-1}$ than the change of C_{ant} in the atmosphere due to the nonlinear carbon chemistry. Small deviations of $C_{ant}^0(t)$ from the exponential fit cause the exact C_{ant} increase rate to depend both on the shape of the TTD (and thus the location) and the reference times for which C_{ant} is calculated. Here, we do

Table 6. C_{ant} accumulation anomalies for the Atlantic Ocean ($\Delta_t C_{ant}^{anom}$) , i. e. deviations between the C_{ant} increase based on tracer data from the actual period and the predicted C_{ant} increase based on tracer data from the previous period.

	$C_{ant}^{2000} - C_{ant}^{1990\to2000}$	$C_{ant}^{2010} - C_{ant}^{2000\to2010}$	$C_{ant}^{2020} - C_{ant}^{2010\to2020}$
North	0.1 ± 1.5	0.2 ± 1.6	-0.1 ± 1.8
South	-1.8 ± 1.8	-0.8 ± 2.1	-0.2 ± 2.3
Total	-1.7 ± 2.9	-0.6 ± 3.4	-0.4 ± 3.6

not extend the exponential fit of $C_{ant}^0(t)$ towards 2020, but infer mean decadal increase rates from the C_{ant} inventories in 1990, 2000, 2010 and 2020 based on all CFC/SF$_6$ data (values in Table 3). The resulting increase is $1.74\,\%\,\mathrm{yr}^{-1}$ for the decade 1990–2000, $1.73\,\%\,\mathrm{yr}^{-1}$ for 2000–2010 and $1.68\,\%\,\mathrm{yr}^{-1}$ for the last period 2010–2020. All values are quite close to the result

510 of $1.69\,\%\,\mathrm{yr}^{-1}$ in *Steinfeldt et al.* (2009). *Gruber et al.* (2019) also inferred an expected C_{ant} change based on the atmospheric CO_2 increase and mean changes in the buffer factor and C_{ant} disequilibrium. The resulting C_{ant} change between 1994 and 2007 was $28\,\%$, or $1.92\,\%\,\mathrm{yr}^{-1}$. The higher value is probably because *Gruber et al.* (2019) considered only the atmospheric CO_2 increase between 1994 and 2007, which is larger than a longer term mean, as the CO_2 growth rate has increased. The C_{ant} increase of the older waters in the ocean interior, however, reflects the smaller rise of atmospheric CO_2 from earlier decades.

515 ### 3.3.2 Deviations of C_{ant} storage from steady state

Here, we come back to the C_{ant} accumulation anomalies $\Delta_t C_{ant}^{anom}$, that have been introduced in section 2.3. The magnitude of these anomalies over the decades 1990–2000, 2000–2010 and 2010–2020 is presented in Table 6. It can also be inferred from Fig. 9 as the difference between the boxes and the horizontal coloured lines, which show the C_{ant} increase based on the decadal forecasts (e. g. $C_{ant}^{1990\to2000} - C_{ant}^{1990}$). In the South Atlantic, $\Delta_t C_{ant}^{anom}$ is negative, especially for the period 1990–2000. This

520 would imply a decrease in C_{ant} storage due to changes in circulation/ventilation. Note, however, that all numbers in Table 6 are not significantly different from zero. Thus, at least for the North and South Atlantic as a whole, the C_{ant} increase over the last 30 years is almost in agreement with the rising atmospheric CO_2. On smaller regional scales, however, there are regions where $\Delta_t C_{ant}^{anom}$ is statistically significantly different from zero (Fig. 12). In general, the local extrema of $\Delta_t C_{ant}^{anom}$ are about $\pm 5\,\mu\mathrm{mol\,kg}^{-1}$, the same magnitude as in (*Gruber et al.*, 2019).

525 The zonal mean section of the C_{ant} accumulation anomaly obtained for the western Atlantic for the periods 1990–2000, 2000–2010 and 2010–2020 (Fig. 12a, c and e) show some areas with extreme values of $\Delta_t C_{ant}^{anom}$ which are similar for all three decadal periods. One is located in the South Atlantic within the AAIW, one in the tropics (20°S–20°N) above the AAIW and one in the North Atlantic in the Central Water, LSW, ISOW and DSOW.

The C_{ant} anomalies in the southwestern Atlantic are most pronounced over the first decade (1990–2000, Fig. 12a). They

530 show negative values south of 40°S between 100 and $1000\,\mathrm{m}$ depth in the AAIW, a positive anomalies directly south and equatorward (south of 20°S) in a slightly shallower depth range within AAIW and the overlying SAMW. A similar structure has been inferred in *Waugh et al.* (2013) from transient tracer data for the southern parts of the Atlantic, Indian, and Pacific

Ocean. These authors ascribe the changes in ventilation to a strengthening and southward movement of the westerly wind belt. This leads to enhanced upwelling of older water with low C_{ant} south of the polar front and increased northward Ekman transport and formation of mode waters (with high C_{ant}) north of the front. A similar dipole in the upper $1000\,\mathrm{m}$ of the South Atlantic is also evident in the study of *Gruber et al.* (2019). *Tanhua et al.* (2017) also found a large C_{ant} storage in SAMW, at least between 1990 and 2005.

The second area with extreme values of $\Delta_t C_{ant}^{anom}$ in the tropical Atlantic is mainly restricted to the layer above $500\,\mathrm{m}$ (subtropical mode water). Positive and negative C_{ant} accumulation anomalies alternate in latitudinal direction and between the decades. They could be a consequence of variable mode water formation in the subtropics. Such changes in the subtropical cell, with enhanced production and southward transport of C_{ant} rich mode water has been inferred from an inverse model in *DeVries et al.* (2017), with enhanced production and equatorward transport of C_{ant} rich mode water in the 1990s. Unfortunately, the study in *DeVries et al.* (2017) ends in 2010, and the decades in which the data are grouped are shifted by 5 years compared to our study, thus prohibiting a direct comparison of the decadal results. Different to our results, *Gruber et al.* (2019) find negative C_{ant} anomalies in the whole tropical Atlantic over the upper $1000\,\mathrm{m}$.

The northern most area with extreme values of $\Delta_t C_{ant}^{anom}$ is located north of 40°N in the subpolar North Atlantic including the Labrador Sea (Fig. 12). This structure reflects the observed variability of convective activity in the Labrador Sea and the associated changes in LSW formation. An unprecedented deep reaching convection formed a very dense mode of LSW from 1987 to 1994 (*Yashayaev*, 2007). During the following years, only lighter modes of LSW (Upper LSW, ULSW) have been formed (*Stramma et al.*, 2004), (*Kieke et al.*, 2006), (*Yashayaev*, 2007) whereas the pool of dense LSW (DLSW) has been exported from the formation region south- and eastward (*Kieke et al.*, 2007), (*Rhein et al.*, 2015). These two processes are reflected in the positive $\Delta_t C_{ant}^{anom}$ for the period 2000–2010 around $1000\,\mathrm{m}$ (formation of ULSW modes) and the negative C_{ant} anomalies between $1500\,\mathrm{m}$ and $2000\,\mathrm{m}$ (export of DLSW) in Fig. 12c. This lack of C_{ant} storage in the deeper part of the LSW between 2000 and 2010 is also visible in Fig. 11c.

In 2008, convection in the Labrador Sea exceeded a depth of $1600\,\mathrm{m}$ again for the first time in years (*Våge et al.*, 2009), but without a great impact on the C_{ant} and oxygen trends (*Rhein et al.*, 2017). In the study by *Gruber et al.* (2019), the C_{ant} anomaly in the North Atlantic is negative down to a depth of $\approx 2500\,\mathrm{m}$ with the minimum in the upper $\approx 1000\,\mathrm{m}$. Thus, a ULSW/DLSW dipole in C_{ant} is not found there. Studies about the convection in the Labrador Sea indicate that at least the upper $500-1000\,\mathrm{m}$ of the water column have been convectively renewed every year since the 1990s (*Yashayaev*, 2007; *Kieke and Yashayaev*, 2015; *Yashayaev and Loder*, 2016), which makes a drastic decrease of the C_{ant} storage in that depth range unlikely. Starting in 2014, deep reaching convection in the Labrador Sea has re-emerged (*Kieke and Yashayaev*, 2015; *Yashayaev and Loder*, 2016). this is reflected by the positive C_{ant} anomaly in the LSW in the northwestern Atlantic between 2010 and 2020. However, the density of this recently formed LSW is still smaller than the density of the LSW originating from the early 1990s (*Yashayaev and Loder*, 2016). Hence, the positive $\Delta_t C_{ant}^{anom}$ values do not reach the lower boundary of the LSW layer. Also the Irminger Sea has been influenced by the enhanced deep convection in the subpolar morthwestern Atlantic, and a large increase in C_{ant} has been found there (*Fröb et al.*, 2016).

In the bottom waters north of $40°N$ (DSOW) there is an alternating pattern of negative and positive $\Delta_t C_{ant}^{anom}$ values (Fig. 12a, c and e). From 1965 to 2000, the overflow waters experienced a freshening trend lasting over more than three decades (*Dickson et al.*, 2002). This long-term trend does not influence the C_{ant} uptake of ISOW and DSOW, as no such signal is evident in Fig. 12. Especially for the DSOW annual fluctuations in salinity (and also temperature) overlay the long-term freshening trend (*Yashayaev*, 2007). These different 'vintages' of DSOW might be the reason for the alternating minima and maxima in $\Delta_t C_{ant}^{anom}$ in the bottom waters north of $35°N$.

In the northeastern Atlantic, the C_{ant} accumulation anomaly in the LSW for the period 2000–2010 is similar to that in the northwestern part, although less pronounced. LSW is formed in the western Atlantic and the $\Delta_t C_{ant}^{anom}$ of the newly formed LSW becomes diluted when the anomalies spread eastward. The recent positive $\Delta_t C_{ant}^{anom}$ value in LSW has not become prominent in the North eastern Atlantic until 2020.

Another small region with a C_{ant} deficit is located within the deep and bottom water (WSDW and AABW) of the southwestern Atlantic around $55°S$ between 1990 and 2000. This is the area where the newly formed deep water originating from the Weddell Sea is advected eastward (see above). This recently ventilated WSDW is relatively high in C_{ant} (Fig. 7a), but only shows a small decadal increase (Fig. 12a), lacking the expected growth from the atmospheric CO_2. This result is in agreement with *Huhn et al.* (2013), who also found an aging and $\Delta_t C_{ant}^{anom}$ deficit of AABW in the Weddell Sea. After 2000, this negative anomaly does not occur anymore, and the C_{ant} increase in WSDW/AABW between $60°$ and $50°S$ is higher (Fig. 11c, e and 12c, e).

Negative C_{ant} accumulation anomalies can also be found in the southeast Atlantic between 2000 and $3000\,m$ depth and $45°$ to $25°S$ in the period 1990–2000. As this negative anomaly is far away from the deep water formation regions, we have no clear explanation for that. One reason could be that the waters present in 1990 are still affected by the Weddell Polynya that has occured in the years 1974, 1975 and 1976 (*Carsey*, 1980) and are thus relatively high in C_{ant}.

4 Summary and Conclusions

We used a modified TTD method allowing for the admixture of old, C_{ant} free waters to access the C_{ant} inventory of the Atlantic, its increase and its variability over the last two decades. In 1990, $43.0 \pm 7.3\,PgC$ of C_{ant} were stored in the total Atlantic. Over the next 30 years, this amount increased to $68.2 \pm 10.8\,PgC$. This increase is mainly caused by the rising atmospheric CO_2 concentrations. Changes in circulation/ventilation have a regional impact on the C_{ant} concentrations, but only a minor effect on the basin wide inventory.

The absolute C_{ant} inventories seem to be similar across the most common methods, like ΔC^*, TTD and GF methods, except for some subregions like the Southern Ocean, where the TTD method yields larger values. However, the incorporation of an explicit dilution into the TTD method leads to C_{ant} concentration that are smaller by more than $5\,\mu mol\,kg^{-1}$ in part of the WSDW and AABW compared to the TTD method without dilution, thus reducing the deviations towards the other methods. Still, discrepancies between the different C_{ant} calculation techniques occur in the vertical distribution of C_{ant}, especially regarding the C_{ant} fraction of the deep ocean. That has repercussions on the conclusions how well and for hpw long C_{ant}

600 is stored in the ocean. A larger Cant storage in deep waters with a long turn over time compared to upper water masses will remove C_{ant} from the atmosphere more enduring.

Our C_{ant} increments for the three decades of $6.4 \pm 2.8\,\mathrm{Pg\,C}$, $8.6 \pm 3.4\,\mathrm{Pg\,C}$, and $10.2 \pm 3.5\,\mathrm{Pg\,C}$ are about 30–40 % of the global values in *Friedlingstein et al.* (2020) of $2.0 \pm 0.5\,\mathrm{Pg\,C\,yr^{-1}}$, $2.1 \pm 0.5\,\mathrm{Pg\,C\,yr^{-1}}$ and $2.5 \pm 0.6\,\mathrm{Pg\,C\,yr^{-1}}$. The Atlantic area considered here makes up $22\,\%$ of the global ocean area. The high C_{ant} concentrations in the North Atlantic due

605 to NADW formation lead to the high contribution of the Atlantic to the global C_{ant} storage compared to its volumetric fraction.

The main discrepancy between this study and others using the eMLR (*Woosley et al.*, 2016) and eMLR(C^*) method (*Gruber et al.*, 2019; *Müller et al.*, 2023) is the regional distribution of the C_{ant} change. Parts of the differences can be explained by the weakness of the non-TTD methods to resolve the C_{ant} changes in the deep ocean. In the global studies by *Gruber et al.* (2019) and *Müller et al.* (2023), the increase of the C_{ant} column inventory in the Atlantic still exceeds that in the Pacific and

610 Indian Ocean, but the global maximum in the North Atlantic is missing. Applying our TTD method, we find a significant C_{ant} increase in the overflow waters (ISOW and DSOW) in the North Atlantic, which contributes to the increase in the column inventory there. On the contrast, in *Woosley et al.* (2016) the deep layers of the North Atlantic are found to be almost stagnant in C_{ant}, and in *Gruber et al.* (2019) and *Müller et al.* (2023) the C_{ant} increase below $3000\,\mathrm{m}$ depth is only considered for the total inventory, not for the C_{ant} distribution. The significant increase of the C_{ant} concentrations in ISOW and DSOW found in

615 our study has not been reported before. Evident through the presence and temporal increase of CFCs in these overflow waters, it is unlikely that these waters have not contributed to the storage of C_{ant} over the last two decades.

Also the C_{ant} accumulation anomaly due to a variable ocean circulation in *Gruber et al.* (2019) opposes our findings. In *Gruber et al.* (2019), this anomaly is mainly positive in the South Atlantic, except for the AAIW layer, and negative in the North Atlantic. In our study, the deep South Atlantic shows a slightly negative C_{ant} accumulation anomaly, and in the north, we

620 find alternating patterns with a positive anomaly in ULSW and negative in DLSW between 2000 and 2010. Using the standard TTDs instead would even lead to a larger C_{ant} deficit in the South Atlantic (see Fig.3e and f and 4e and f) due to the higher "expected" CFC increase with time (Fig. 5).

The patterns of the C_{ant} accumulation anomalies found here mainly follow the changes in water mass age/ventilation that have already been described in previous studies, e, g. for the Southern Ocean (*Waugh et al.*, 2013; *Huhn et al.*, 2013), and the

625 changes in the convective activity in the Labrador Sea (*Kieke et al.*, 2007; *Yashayaev*, 2007; *Yashayaev and Loder*, 2016). All these studies are based on the variability of hydrographic properties and/or anthropogenic tracers. The large C_{ant} accumulation anomaly in the old waters of the South Atlantic, as found in *Gruber et al.* (2019) is not reflected in hydrographic changes. It is also unlikely, as property anomalies in the ocean are typically large near the water mass formation regions and decay downstream towards the old waters in the ocean interior.

630 The investigation of oceanic circulation/ventilation variability and its impact on anthropogenic carbon storage is of importance for both the understanding of the mechanisms of the recent variability in oceanic carbon uptake (*DeVries et al.*, 2019) and the estimation of the future evolution of the oceanic carbon sink in a changing climate. In the future, also changes in the biogenic carbon or carbon/climate feedbacks, i. e. outgassing of CO_2 in a warming ocean may play a larger role. Our results

show that a decoupling of the atmospheric C_{ant} increase and the increase in the Atlantic C_{ant} storage has not yet been achieved by the observed decadal variability in water mass ventilation and circulation.

Data availability. Data are available at https://www.ncei.noaa.gov/data/oceans/ncei/ocads/data/0283442/ (GLODAPV2.2023) and https://www.bodc.ac.uk/geotraces/data/idp2017/ (GEOTRACES section GA02). The data of the additional cruises are available via PAN-GAEA

MSM64: https://doi.org/10.1594/PANGAEA.962044,

MSM73: https://doi.pangaea.de/10.1594/PANGAEA.911234. The gridded C_{ant} fields form *Sabine et al.* (2004) and *Khatiwala et al.* (2013) were downloaded from https://www.nodc.noaa.gov/ocads/oceans/glodap/GlopDV.html

and http://kelvin.earth.ox.ac.uk/spk/Research/AnthropogenicCarbon/ respectively.

Appendix A: Isopycnal Interpolation of Profiles

The boundaries for the isopycnal interpolation of the single profiles as described in the main section are given in Table 1. For most of the cruises used here, also CTD data would be available. However, we decided to stay with the bottle data from GLODAPv2.2023 for salinity, potential temperature, and to infer the layer thicknesses. One reason is that in GLODAP, also salinity and thus density are quality controlled. We calculated the difference between the layer thicknesses inferred from CTD and bottle data for a cruise where both are available. The root-mean-square error of the layer thicknesses is about $40\,\mathrm{m}$. If one assumes a maximal C_{ant} difference over this depth range of about $20\,\mu\mathrm{mol\,kg}^{-1}$ (from Fig. 6), the difference in the C_{ant} column inventory would be $\approx 40\,\mathrm{m} \cdot 20\,\mu\mathrm{mol\,kg}^{-1} \cdot 1000\,\mathrm{kg\,m}^{-3} = 0.8\,\mathrm{mol\,m}^{-2}$. That is about $1\,\%$ of the total C_{ant} column inventory (see Fig. 5, between 30 and $180\,\mathrm{mol\,m}^{-2}$). The error of the layer thicknesses is randomly (in some cases the layer with the higher C_{ant} concentration is too thick, in other cases too thin). Due to the large number of profiles (> 1000), the total error is much smaller than $1\,\%$.

Appendix B: CFC and SF$_6$ saturation

The CFC and SF_6 saturations assumed for the different density layers are given in Table A1. They decrease from $100\,\%$ in the upper waters to $80\,\%$ in deep waters. For most cruises, the surface is close to saturation, both for CFCs and SF_6. Hence, a saturation of $100\,\%$ for the upper layers seems to be reasonable. For the deep layers, the saturation of the surface waters at the time of deep water formation, i. e. late winter/early spring needs to be known. Most cruises from higher latitudes, however, are from late spring until autumn, avoiding the severe winter conditions. In order to estimate the saturation of newly formed North Atlantic Deep Water, Fig. B1 shows the CFC-12 and SF_6 data from the western subpolar North Atlantic (Labrador Sea and Irminger Sea respectively) below $500\,\mathrm{m}$ depth for two different years, expressed as saturation with respect to the solubility equilibrium. This has been calculated by using the observed pot. temperature, salinity, and the atmospheric tracer concentration from the year of observation. Waters with the highest saturation point to remnants from the last winter convection, waters with

Table A1. Boundaries of density layers and assumed saturation for CFCs and SF$_6$ in every layer.

	density [kgm^{-3}]	CFC/SF$_6$-saturation [%]		density [kgm^{-3}]	CFC/SF$_6$-saturation [%]		density [kgm^{-3}]	CFC/SF$_6$-saturation [%]
σ_θ	0		σ_θ	27.6		$\sigma_{1.5}$	34.77	
		100			95			80
σ_θ	24		$\sigma_{1.5}$	34.42		σ_4	45.8	
		100			92.5			80
σ_θ	25		$\sigma_{1.5}$	34.5		σ_4	45.83	
		100			90			80
σ_θ	25.5		$\sigma_{1.5}$	34.55		σ_4	45.86	
		100			87.5			80
σ_θ	26		$\sigma_{1.5}$	34.6		σ_4	45.88	
		100			85			80
σ_θ	26.5		$\sigma_{1.5}$	34.625		σ_4	45.9	
		100			85			80
σ_θ	26.8		$\sigma_{1.5}$	34.65		σ_4	45.925	
		97.5			85			80
σ_θ	27		$\sigma_{1.5}$	34.675		σ_4	45.95	
		95			85			80
σ_θ	27.15		$\sigma_{1.5}$	34.7		σ_4	45.975	
		95			82.5			80
σ_θ	27.3		$\sigma_{1.5}$	34.725		σ_4	46	
		95			80			80
σ_θ	27.4		$\sigma_{1.5}$	34.75		σ_4	46.025	
		95			80			80
σ_θ	27.5		$\sigma_{1.5}$	34.77		σ_4	46.95	
		95						80
σ_θ	27.6					σ_4	46.1	
								80
						σ_4	46.15	
								80
						σ_4	46.2	
								80
						σ_4	50	

lower saturations are a mixture of recently ventilated and older water. This interpretation is different from *Raimondi et al.* (2021), where the mean tracer concentration in the core layer of newly formed LSW after convection is used to infer the saturation.

In 1994, mainly the denser mode of LSW has been ventilated, between $\sigma_{1.5} = 34.65\,\mathrm{kg\,m}^{-3}$ and $\sigma_{1.5} = 34.7\,\mathrm{kg\,m}^{-3}$. In 2013, the ventilation only reached densities above $\sigma_{.5} = 34.6\,\mathrm{kg\,m}^{-3}$. The highest saturations in the ventilated density range are between 80% and 100% for both years. The SF$_6$ saturation in 2013 is only slightly below the values for CFC-12.

The overflow waters are not directly formed in the subpolar North Atlantic, but originate from the Nordic Seas. However, they are modified after passing the Greenland-Scotland-Ridge, e. g. the ISOW entrains Labrador Sea Water and Northeast Atlantic Water (*LeBel et al.*, 2008), and the DSOW warm and saline Atlantic Water and fresher water from the East Greenland Current (*Jochumsen et al.*, 2015). The tracer saturation of the overflow waters ($\sigma_4 > 45.8\,\mathrm{kg\,m}^{-3}$) in the Irminger Sea, downstrem of the entrainment, are shown in Fig. B1 for data prior and after the year 2000. The saturation is even higher for the earlier period, probably due to short-term variability of the properties of the overflow waters (*Yashayaev*, 2007; *Jochumsen et al.*, 2015). The maximum is around 80%, but most data points have a smaller saturation. Note, however, that the Irminger Sea is located downstream of the formation area, hence the overflow waters there is not newly formed, but has already been subject to aging and dilution, which reduces the apparent CFC saturation. In Fig. S1 also the tracer saturation from Table S1 is depicted,

including the assumed error of 10%. The saturation of 85% for the major part of the LSW density range is identical with the
value used in *Kieke et al.* (2006), *Kieke et al.* (2007), *Steinfeldt et al.* (2009). For the DSOW, the applied saturation of 80% is
significantly larger than the 65% from *Steinfeldt et al.* (2009) but close to the value of 75% from *Swift et al.* (1980), *LeBel et al.* (2008).

Appendix C: Temporal evolution of anthropogenic tracers

Fig. C1 shows the concentration of of CFC-11, CFC-12 and SF_6 in the northern hemispheric atmosphere and of tritium in North
Atlantic surface waters as a function of time. The tritium curve for the North Atlantic from Dreisigacker and Roether (1978) is
continued assuming radioactive decay after 1978. Atmospheric CFC and SF_6 concentration are adopted from *Bullister* (2017)
and extrapolated linearly in time for the last five years.

Appendix D: Variation of TTD Parameters

The effect of the choice of the TTD parameters on the shape of the TTD and the inferred C_{ant} concentration is illustrated in
Fig. D1 and Table C1. We assume a CFC-12 concentration of $0.4\,\mathrm{pmol\,kg^{-1}}$ observed in 2010, a CFC-saturation of 0.85, a
potential temperature of $\theta = 3°C$ and a salinity of $S = 34.9$. C_{ant} is calculated for the reference year 2010 and an alkalinity of
$2308\,\mu\mathrm{mol\,kg^{-1}}$ (the value derived from *Lee et al.* (2006) for the North Atlantic). The maximum of the TTD occurs at younger
ages for $\Delta/\Gamma = 2$ compared to the case with $\Delta/\Gamma = 1$. This is a quite general behaviour, i. e. increasing the Δ/Γ ratio leads
to a younger age of the mode of the TTD. Reducing the fraction of young water leads to an even younger mode, although in
this case the Δ/Γ ratio is always chosen as one. The younger the mode of the possible TTDs derived from a given CFC-12
concentration, the smaller is the inferred C_{ant} concentration (see Table D1).

The TTD $\mathcal{G}_{young}$ for the young water in Figure D1 only represents half of the water, as the fraction f in this example equals
0.5. To illustrate how the complete TTD might look like, we assume an old TTD $\mathcal{G}_{old}$ with $\Gamma = 500\,\mathrm{yr}$ and $\Delta = 250\,\mathrm{yr}$. The
sum of $\mathcal{G}_{young}$ and $\mathcal{G}_{old}$ is shown as dashed line in Figure D1. This choice of the parameters for $\mathcal{G}_{old}$ is arbitrary, but it fulfills
the condition that the inferred C_{ant} concentration is small ($< 0.5\,\mu\mathrm{mol\,kg^{-1}}$ in this case) and thus might be neglected. The
sum of $\mathcal{G}_{young}$ and $\mathcal{G}_{old}$ only has one clear maximum. The mode of $\mathcal{G}_{old}$ is much less pronounced than that of $\mathcal{G}_{young}$, so the
complete TTD has a kind of saddle point around the mode of $\mathcal{G}_{old}$ ($250\,\mathrm{yr}$ in the example in Figure D1).

Appendix E: Relative C_{ant} change ($\Delta_t C_{ant}$) between 1990 and 2020

Fig. E1 shows the relative increase in the C_{ant} column inventory for the periods 1990–2000, 2000–2010, and 2010–2020. In
contrast to that, in Fig. 12 from the main section the absolute values of the C_{ant} increase are shown. From the rising atmospheric
CO_2 concentration and a steady state ocean, a decadal increase of the C_{ant} inventory of about 19% would be expected.

Table D1. TTD parameters derived for a CFC-12 concentration of $0.2\,\mathrm{pmol\,kg^{-1}}$ in 2010, assuming a CFC-saturation of 0.85, a potential temperature of $\theta = 3^\circ\mathrm{C}$ and a salinity of $S = 34.9$. C_{ant} is calculated for the reference year 2010 and an alkalinity of $2308\,\mu\mathrm{mol\,kg^{-1}}$ (the value derived form *Lee et al., 2006* for the North Atlantic). Also given is the fraction of water older than $200\,\mathrm{yr}$.

	$\Gamma\,[\mathrm{yr}]$	$\Delta\,[\mathrm{yr}]$	$C_{\mathrm{ant}}\,[\mathrm{pmol\,kg^{-1}}]$	$f > 200\,yr$	
$\Delta/\Gamma = 1\,\mathrm{f} = 1$	178.5	178.5	14.0	0.26	[a] Values are for the young TTD component only.
$\Delta/\Gamma = 2\,\mathrm{f} = 1$	564.5	1129	12.5	0.38	
$\Delta/\Gamma = 1\,\mathrm{f} = 0.5$	104.5^{a}	104.5^{a}	10.4	0.13^{a}	

Author contributions. R.S. carried out the calculations of anthropogenic carbon and prepared the manuscript with contributions from both coauthors.

Competing interests. None.

710 *Acknowledgements.* We thank the captains, crews and scientific partcipants of the numerous research cruises whose data have contributed to this work. The cruises SUBPOLAR08, M82/2, M85/1, MSM21/2, MSM27, MSM28, MSM38, and MSM39 have been conducted in the framework of programs funded by the German Federal Ministery for Education and Research (BMBF) (Cooperative Projects "Nordatlantik" and "RACE" (grants03F0443C, 03F0605C and 03F0651C to M. Rhein)). K. Bulsiewicz (IUP at Univerity of Bremen) measured the CFC and SF_6 samples obtained from the cruises conducted by IUP Bremen. M. Rhein received funding from the German Research Foundation
715 (DFG, grants RH 25/36-1, RH 25/36-2, and RH 25/36-3).

References

Álvarez, M., Pérez, F., Bryden, H. L., and Ríos, A.:. Physical and biogeochemical transports structure in the North Atlantic subpolar gyre, J. Geophys. Res.: Oceans, 109, C03027, https://doi.org/10.1029/2003JC002015, 2004.

Brambilla, E. & Talley, L. D. (2008). Subpolar Mode Water in the northeastern Atlantic: 1. Averaged properties and mean circulation. *J. Geophys. Res.: Oceans, 113*, C04025, https://doi.org/10.1029/2006JC004062

Bullister, J., Rhein, M., and Mauritzen, C.: Deep Water Formation. In: Ocean Circulation and Climate - Observing and Modelling the Global Ocean, second edition, edited by G. Siedler, J. Church, J. Gould and S. Griffies, Academic Press, Oxford, ISBN 978-0-12-391851-2, 2013.

Bullister, J. L.: Atmospheric histories (1765–2015) for CFC-11, CFC-12, CFC-113, CCl4, SF6 and N2O. Oak Ridge, Tennessee: Carbon Dioxide Information Analysis Center. Oak Ridge National Laboratory, US Department of Energy, 2017.

Carsey, F. D.:Microwave observations of the Weddell Polynya. Month Weather Rev 108(5):2032–2044, 1980.

Clement, D., and Gruber, N.: The eMLR(C*) method to determine decadal changes in the global ocean storage of anthropogenic CO_2, Global Biogeochem. Cy., 32, 654—679, https://doi.org/10.1002/2017GB005819, 2018.

DeVries, T., Holzer, M., and Primeau, F.: Recent increase in oceanic carbon uptake driven by weaker upper-ocean overturning, Nature, 542, 215–218, https://doi.org/10.1038/nature21068, 2017.

DeVries, T., Le Quéré, C., Andrews, O., Berthet, S., Hauck, J., Ilyina, T., Landschützer, Lenton, A., Lima, I. D., Nowicki, M., Schwinger, J., and Roland Séférian, R.: Decadal trends in the ocean carbon sink, PNAS, 116(24), 11646–11651, https://doi.org/10.1073/pnas.1900371116, 2019.

Dickson, B., Yashayaev, I., Meincke, J., Turrell, B., Dye, S., and Holfort, J.; Rapid freshening of the deep North Atlantic Ocean over the past four decades, Nature, 416, 832–837, https://doi.org/10.1038/416832a. 2002.

Dreisigacker, E., and Roether, E.: Tritium and [99]Sr in North Atlantic surface water, Earth Planet. Sci. Lett., 38, 301–312, 1978.

Fischer, J., Rhein, M., Schott, F. and Stramma, L.: Deep water masses and transports in the Vema Fracture Zone, Deep-Sea Res. I, 43(7) 1067–1074, https://doi.org/10.1016/0967-0637(96)00044-1, 1996.

Fleischmann, U., Hildebrandt, H., Putzka, A. and Bayer, R.: Transport of newly ventilated deep water from the Iceland Basin to the West European Basin, Deep-Sea Res. I, 48(8) 1793–1819, https://doi.org/10.1016/S0967-0637(00)00107-2, 2001.

Friedlingstein, P. et al. (2020). Global Carbon Budget 2020, Earth Syst. Sci. Data, 12, 3269–3340, https://doi.org/10.5194/essd-12-3269-2020, 2020.

Friis, K., Körtzinger, A., Pätsch, J., and Wallace, D.: On the temporal increase of anthropogenic CO_2 in the subpolar North Atlantic, Deep-Sea Res. I, 52(5), 681–698, https://doi.org/10.1016/j.dsr.2004.11.017, 2005.

Fröb, F., Olsen, A., Våge, K., Moore, G. W. K., Yashayaev, Y., Jeansson, E. and Rajasakaren, B.: Irminger Sea deep convection injects oxygen and anthropogenic carbon to the ocean interior, Nat. Commun., 7, 13244, https://doi.org/10.1038/ncomms13244, 2016.

Gruber, N., Sarmiento, J. L., and Stocker, T. F.: An improved method for detecting anthropogenic C_2 in the oceans, Global Biogeochem. Cy., 10,(4), 809–837, https://doi.org/10.1029/96GB01608, 1996.

Gruber, N., Clement, D., Carter, B. R., Feely, R. A., van Heuven, S., Hoppema, M. et al.: The oceanic sink for anthropogenic CO_2 from 1994 to 2007, Science, 363, 1193-–1199, doi: 10.1126/science.aau5153, 2019.

Hall, T. M., Haine, T. W. N., and Waugh, D. W.: Inferring the concentration of anthropogenic carbon in the ocean from tracers, Global Biogeochem. Cy., 16(GB1131), https://doi.org/10.1029/2001GB001835, 2002.

He, Y.-C., Tjiputra, J., Langehaug, H. R., Jeansson, E., Gao, Y., Schwinger, J., and Olsen, A.: A model-based evaluation of the inverse Gaussian transit-time distribution method for inferring anthropogenic carbon storage in the ocean, J. Geophys. Res.: Oceans, 123, 1777–1800, https://doi.org/10.1002/2017JC013504, 2018.

755 Heinze, C., Meyer, S., Goris, N., Anderson, L., Steinfeldt, R., Chang, N., Le Quéré, C., and Bakker, D. C. E.: The ocean carbon sink – impacts, vulnerabilities and challenges, Earth Syst. Dynam., 6, 327–358, https://doi.org/10.5194/esd-6-327-2015, 2015.

Holzer, M., and Hall, T. M.: Transit-time and tracer age distributions in geophysical flows, J. Atmos. Sci., 57, 3539-–3558, 2000.

Huhn, O., Rhein, M., Hoppema, M., and van Heuven, S.: Decline of deep and bottom water ventilation and slowing down of anthropogenic carbon storage in the Weddell Sea, 1984–2011, Deep-Sea Res. I, 76, 66–84, https://doi.org/10.1016/j.dsr.2013.01.005, 2013.

760 Iudicone, D., Speich, S., Gurvan, M. and Blanke, B.: The Global Conveyor Belt from a Southern Ocean Perspective, J. Phys. Oceanogr., 38, 1401–1425, https://doi.org/10.1175/2007JPO3525.1, 2008.

Jochumsen, K., Köllner, M., Quadfasel, D., Dye, S., Rudels, B., and Valdimarsson, H.: On the origin and propagation of Denmark Strait overflow water anomalies in the Irminger Basin, J. Geophys. Res.: Oceans, 120, 1841–1855, https://doi.org/10.1002/2014JC010397, 2015.

765 Khatiwala, S., Tanhua, T., Mikaloff Fletcher, S., Gerber, M., Doney, S. C., Graven, H. D., Gruber, N., McKinley, G. A., Murata, A., and Sabine, C. L.: Global storage of anthropogenic carbon, Biogeosciences, 10, 2169–2191, https://doi.org/10.5194/bg-10-2169-2013, 2013.

Kieke, D., Rhein, M., Stramma, L., Smethie Jr., W. M., LeBel, D. A., and Zenk, W.: Changes in the CFC inventories and formation rates of Upper Labrador Sea Water, 1997–2001, J. Phys. Oceanogr., 36(1), 64–86, https://doi.org/10.1175/JPO2814.1, 2006.

Kieke, D., Rhein, M., Stramma, L., Smethie Jr., W. M., Bullister, J. L., and LeBel, D. A.: Changes in the pool of Labrador Sea Water in the
770 subpolar North Atlantic, Geophys. Res. Lett., 34, L06605, https://doi.org/10.1029/2006GL028959, 2007.

Kieke, D., and Yashayaev, I.: Studies of Labrador Sea Water formation and variability in the subpolar North Atlantic in the light of international partnership and collaboration, Prog. Oceanogr., 132(3), 220–232, https://doi.org/10.1016/j.pocean.2014.12.010, 2015.

Klatt, O., Roether, W., Hoppema, M., Bulsiewicz, K., Fleischmann, U., Rodehacke, C., Fahrbach, R., Weiss, R. F., and Bullister, J. L.: Repeated CFC sections at the Greenwich Meridian in the Weddell Sea, J. Geophys. Res.: Oceans, 107(C4), 3030,
775 https://doi.org/10.1029/2000JC000731, 2002.

Lauvset, S. K., Lange, N., Tanhua, T., Bittig, H. C., Olsen, A., Kozyr, Álvarez, M., Azetsu-Scott,A., Brown, P. J., Carter, B. R., da Cunha, L. C., Hoppema, M., Humphreys, M. P., Ishii, M., Jeansson, E., Murata, A., Müller, J. D., Pérez, F. F., Schirnick, C., Steinfeldt, R., Suzuki, T., Ulfsbo, A., Velo, A., Woosley, R. J., and Key. R.: The annual update GLODAPv2.2023: the global interior ocean biogeochemical data product, Earth Syst. Sci. Data. [preprint], https://doi.org/10.5194/essd-2023-468, accepteg, 2024.

780 Lazier, J., Hendry, R., Clarke, A., Yashayaev, I., and Rhines, P.: Convection and restratification in the Labrador Sea, 1990-–2000, Deep-Sea Res. I, 49(10), 1819–1835, https://doi.org/10.1016/S0967-0637(02)00064-X, 2002.

Lebel, D. A., Smethie Jr., W. M., Rhein, M., Kieke, D., Fine, R. A., Bullister, J. L., Min, D. H., Roether, W., Weiss, R., Andrié, C., Smythe-Wright, D., and and Jones, E. P.: The formation rate of North Atlantic Deep Water and Eighteen Degree Water calculated from CFC-11 inventories observed during WOCE, Deep-Sea Res. I, 55(8) 901–910, https://doi.org/10.1016/j.dsr.2008.03.009, 2008.

785 Le Bras, I. A., Yashayaev, I., and Toole, J. M.: Tracking Labrador Sea Water property signals along the Deep Western Boundary Current, J. Geophys. Res.: Oceans, 122, 5348–5366, https://doi.org/10.1002/2017JC012921, 2017.

Lee, K., Tong, L. T., Millero, F. J., Sabine, C. L., Dickson, A. G., Goyet, C., Park, G. H., Wanninkhof, R., Feely, R. A., and Key, R. M.: Global relationships of total alkalinity with salinity and temperature in surface waters of the world's oceans, Geophys. Res. Lett., 33, L19605, https://doi.org/10.1029/2006GL027207, 2006.

790 Mauritzen, C., Price, J., Sanford, T., and Torres, D.: Circulation and mixing in the Faroese Channels, Deep Sea Res., Part I, 52(6), 883-–913, https://doi.org/10.1016/j.dsr.2004.11.018, 2005.

McCartney, M. S.: The subtropical recirculation of mode waters, J. Mar. Res.,40, 427-–464, 1982.

McCartney, M. S.: Recirculating components to the deep boundary current of the northern North Atlantic, Prog. Oceanogr., 29, 283–383, https://doi.org/10.1016/0079-6611(92)90006-L, 1992.

795 Mercier, H., and Morin, P.; Hydrography of the Romanche and Chain Fracture Zones, J. Geophys. Res.: Oceans, 102, C5, 10373–10389, https://doi.org/10.1029/97JC00229, 1997.

Müller, J. D., Gruber, N., Carter, B., Feely, R., Ishii, M., Lange, N., Lauvset, S. K., Murata, A., Olsen, A., Pérez, F. F., Sabine, C., Tanhua, T., Wanninkhof, R., and Zhu, D.: Decadal Trends in the Oceanic Storage of Anthropogenic Carbon From 1994 to 2014, AGU Adv., 4, e2023AV000875, https://doi.org/10.1029/2023AV000875, 2023.

800 Orsi, A. H., Johnson, G. C., and Bullister, J. L.: Circulation, mixing, and production of Antarctic Bottom Water, Prog. Oceanogr., 43, 55-–109, https://doi.org/10.1016/S0079-6611(99)00004-X, 1999.

Pérez, F. F., Vázquez-Rodríguez, M., Mercier, H., Velo, A., Lherminier, P., and Ríos, A. F.: Trends of anthropogenic CO_2 storage in North Atlantic water masses, Biogeosciences 7, 1789–1807, https://doi.org/10.5194/bg-7-1789-2010, 2010.

Pérez, F. F., Mercier, H., Vázquez-Rodríguez, M., Lherminier, P., Velo, A., Pardo, P. C., Roson, G., and Ríos, A. F.: At-
805 lantic Ocean CO_2 uptake reduced by weakening of the meridional overturning circulation, Nature Geoscience, 6(2), 146–152, https://doi.org/10.1038/ngeo1680, 2013.

Petit, T., Mercier, H., and Thierry, V.: First direct estimates of volume and water mass transports across the Reykjanes Ridge, J. Geophys. Res.: Oceans, 123, 6703-—6719, https://doi.org/10.1029/2018JC013999, 2018.

Polzin, K. L. Toole, J. M., Ledwell, J. R., and Schmitt, R. W.: Spatial variability of turbulent mixing in the abyssal ocean, Science, 276,
810 93–96, 1997.

Raimondi, L., Tanhua, T., Azetsu-Scott, K., Yashayaev, I., and Wallace, D. W. R.: A 30 -Year Time Series of Transient Tracer-Based Estimates of Anthropogenic Carbon in the Central Labrador Sea, J. Geophys. Res. Oceans, 126, e2020JC017092, https://doi.org/10.1029/2020JC017092, 2021.

Rhein, M., and Stramma, L.: Seasonal fluctuations in the Deep Western Boundary Current around the eastern tip of Brazil. Deep-Sea Res. I,
815 52(8), 1414–1428, https://doi.org/10.1016/j.dsr.2005.03.004, 2005.

Rhein, M., Kieke, D., and Steinfeldt, R.: Ventilation of the Upper Labrador Sea Water, 2003–2005, Geophys. Res. Lett., 34, L06603, doi:10.1029/2006GL028540, 2007. *Deep-Sea Res. I, 52*(8), 1414–1428.

Rhein, M., Kieke, D., and Steinfeldt, R.: Advection of North Atlantic Deep Water from the Labrador Sea to the southern hemisphere, J. Geophys. Res.: Oceans, 120, 2471–2487, https://doi.org/10.1002/2014JC010605,2015.

820 Rhein, M., Steinfeldt, R., Kieke, D., Stendardo, I., and Yashayaev, I.: Ventilation variability of Labrador Sea Water and its impact on oxygen and anthropogenic carbon, Phil. Trans. R. Soc. A 375(2102), https://doi.org/10.1098/rsta.2016.0321, 2017.

Rhein, M., Steinfeldt, R., Huhn, O., Sültenfuß, J., and Breckenfelder, T.: Greenland subarine melt water observed in the Labrador and Irminger Sea, Geophys. Res. Lett., 45, 10.570-10.578, https://doi.org/10.1029/2018GL079110, 2018.

Ríos, A. F., Velo, A., Pardo, P. C., Hoppema, M., and Pérez, F. F.: An update of anthropogenic CO_2 storage rates in the western South
825 Atlantic basin and the role of Antarctic Bottom Water, J. Mar. Sys., 94, 197–203, https://doi.org/10.1016/j.jmarsys.2011.11.023, 2012.

Sabine, C. L., Feely, R. A., Gruber, N., Key, R. M., Lee, K., Bullister, J. L., R. Wanninkhof, Wong, C. S., Wallace, D. W. R., Tilbrook, B., Millero, F. J., Peng, T. H., Kozyr, A., Ono, T., and Rios, A. F: The oceanic sink for anthropogenic CO_2, Nature, 305, 367–371, DOI: 10.1126/science.1097403, 2004.

Schlitzer, R., Anderson, R. F., Masferrer Dodas, E., et al.: The GEOTRACES Intermediate Data Product 2017, Chem. Geol. 493, 210–223,
830   https://doi.org/10.1016/j.chemgeo.2018.05.040, 2018.

Smethie, W. M. Jr., and Swift, J. H.: The tritium:Krypton-85 age of Denmark Strait Overflow Water and Gibbs Fracture Zone Water just south of Denmark Strait, J. Geophys. Res.: Oceans, 94, 8265–8275, https://doi.org/10.1029/JC094iC06p08265, 1989.

Smethie W. M. Jr., Fine, R. A., Putzka, A., and Jones, E. P.: Tracing the flow of North Atlantic Deep Water using chlorofluorocarbons, J. Geophys. Res., 105(C6), 14,297–14,323, https://doi.org/10.1029/1999JC90027, 2000.

835   Smith, J. N., McLaughlin, F. A., Smethie Jr., W. M., Moran, S. B., Lepore ,K.: Iodine-129, ^{137}Cs, and CFC-11 tracer transit time distributions in the Arctic Ocean, J. Geophys. Res.,116, C04024, https://doi.org/10.1029/2010JC006471, 2011.

Steinfeldt, R., and Rhein, M.: Spreading velocities and dilution of North Atlantic Deep Water in the tropical Atlantic based on CFC time series, J. Geophys. Res.: Oceans, 109(C3), C03046, https://doi.org/10.1029/2003JC002050, 2004.

Steinfeldt, R., Rhein, M., Bullister, J. L., and Tanhua, T.: Inventory changes in anthropogenic carbon from 1997–2003 in the Atlantic Ocean
840   between 20°S and 65°N, Global Biogeochem. Cycles, 23, GB3010, https://doi.org/10.1029/2008GB003311, 2009.

Stramma, L., Kieke, D., Rhein, M., Schott, F., Yashayaev, I., and Koltermann, K. P.: Deep Water changes at the western boundary of the subpolar North Atlantic during 1996 to 2001, Deep-Sea Res. I, 51(8), 1033–1056, https://doi.org/10.1016/j.dsr.2004.04.001, 2004.

Swift, J. H., Aagaard, D., and Malmberg , S. V: The contribution of the Denmark Strait Overflow to the deep North Atlantic, Deep Sea Res., 27, 29–42, https://doi.org/10.1016/0198-0149(80)90070-9, 1980.

845   Sy, A., Rhein, M., Lazier, J. R. N., Koltermann, K. P., Meincke, J., Putzka, A., and Bersch, M.: Surprisingly rapid spreading of newly formed intermediate waters across the North Atlantic Ocean, Nature, 386, 675—679, 1997.

Talley, L. D.: Some aspects of ocean heat transport by the shallow, intermediate and deep overturning circulations, in: Mechanisms of Global Climate Change at Millennial Time Scales (eds P.U. Clark, R.S. Webb and L.D. Keigwin), ISBN: 9781118664742, https://doi.org/10.1029/GM112p0001, 1999.

850   Tanhua, T., Bulsiewicz, K., and Rhein, M.: Spreading of Overflow Water from the Greenland to the Labrador Sea, Geophys. Res. Lett., 32 (10), L10605, https://doi.org/10.1029/2005GL022700, 2005.

Tanhua, T., Waugh, D. W., and Wallace, D. W. R.: Use of SF_6 to estimate anthropogenic CO_2 in the upper ocean, J. Geophys. Res.: Oceans, 113, C04037, https://doi.org/10.1029/2007JC004416, 2008.

Tanhua, T., Hoppema, M., Jones, E. M., Stöven, T., Hauck, J., Dávila, M. G., Santana-Casiano, M., Álvarez, M., and Strass, V. H.: Tem-
855   poral changes in ventilation and the carbonate system in the Atlantic sector of the Southern Ocean, Deep–Sea Res. II, 138, 26—38, https://dx.doi.org/10.1016/j.dsr2.2016.10.004, 2017.

van Heuven, S. M. A. C, Hoppema, M., Huhn, O., Slagter, H. A., and de Baar, H. J. W.: Direct observation of increasing CO_2 in the Weddell Gyre along the Prime Meridian during 1973–2008, Deep-Sea Res. II, 58(25–26), 2613–2635, https://doi.org/10.1016/j.dsr2.2011.08.007, 2011.

860   Vázquez-Rodríguez, M. Touratier, F., Lo Monaco, C., Waugh, D. W., Padin, X. A., Bellerby, R. G. J., Goyet, C., Metzl, N., Ríos , A. F., and Pérez, F. F.: Anthropogenic carbon distributions in the Atlantic Ocean: data-based estimates from the Arctic to the Antarctic, Biogeosciences, 6, 439–451, https://doi.org/10.5194/bg-6-439-2009, 2009.

Våge, K., Pickart, R. S., Thierry, V., Reverdin, G., Lee, C. M., Petrie, B., Agnew, T. A., Wong, A., and Ribergaard, H. M.: Surprising return of deep convection to the subpolar North Atlantic Ocean in winter 2007--2008, Nature Geoscience, 2, 67–72, https://doi.org/10.1038/ngeo382, 2009.

Wanninkhof, R., Doney, S. C., Bullister, J. L., Levine, N. M., Warner, M., and Gruber, N.: Detecting anthropogenic CO_2 changes in the interior Atlantic Ocean between 1989 and 2005, J. Geophys. Res.: Oceans, 115, C11028, https://doi.org/10.1029/2010JC006251, 2010.

Watson, A. J., Messias, M. J., Fogelqvist, E., Van Scoy, K. A., Johannessen, T., Oliver, K. I. C., Stevens, D. P., Rey, F., Tanhua, T., and Olsson, K. A.: Mixing and convection in the Greenland Sea from a tracer-release experiment, Nature, 401(6756), 902–904, https://doi.org/10.1038/44807, 1999.

Waugh, D. W., Haine, T. W. N., and Hall, T. M.: Transport times and anthropogenic carbon in the subpolar North Atlantic Ocean, Deep-Sea Res. I, 51, 1475–1491, https://doi.org/10.1016/j.dsr.2004.06.011, 2004.

Waugh, D. W., Hall, T. M., McNeil, I., Key, R., and Matear, R. J.: Anthropogenic CO_2 in the oceans estimated using transit time distributions, Tellus, 58B(5), 376–389, doi:10.1111/j.1600-0889.2006.00222.x, 2006.

Waugh, D. W., Primeau, F., DeVries, T., and Holzer, M.: Recent Changes in the Ventilation of the Southern Oceans, Science, 339, 568–570, doi:10.1126/science.1225411, 2013.

Woosley, R. J., F. J. Millero, and Wanninkhof, R.: Rapid anthropogenic changes in CO_2 and pH in the Atlantic Ocean: 2003—2014, Global Biogeochem. Cy., 30, 70--90, https://doi.org/10.1002/2015GB005248, 2016.

Yashayaev, I.: Hydrographic changes in the Labrador Sea, 1960–2005, Prog. Oceanogr., 73, 242–276, https://doi.org/10.1016/j.pocean.2007.04.015, 2007.

Yashayaev. I., van Aken, H. M., Holliday, N. P., and Bersch. M.: Transformation of the Labrador Sea Water in the subpolar North Atlantic, Geophys. Res. Lett., 34, L22605, https://doi.org/10.1029/2007GL031812, 2007.

Yashayaev, I., and Loder, J. W.: Recurrent replenishment of Labrador Sea Water and associated decadal-scale variability, J. Geophys. Res.: Oceans, 121, 8095—8114, https://doi.org/10.1002/2016JC012046, 2016.
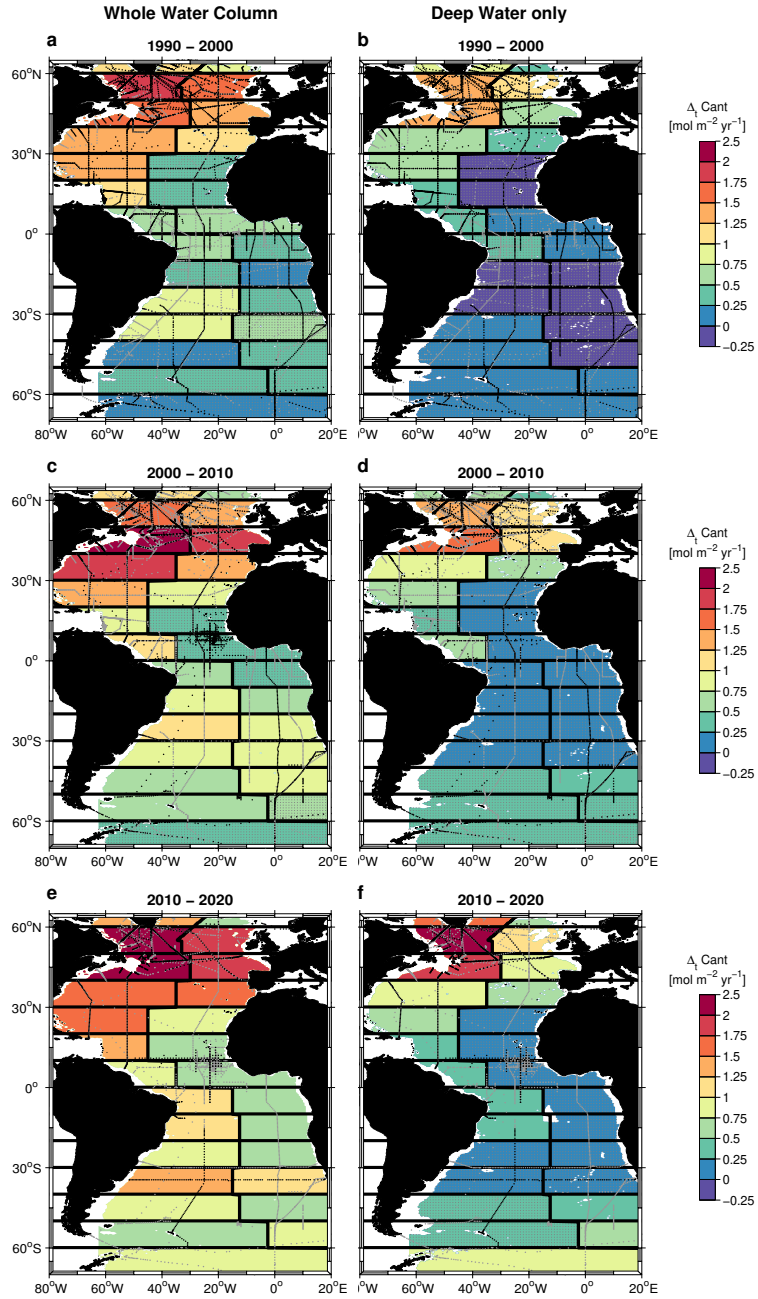
Figure 10. Mean C_{ant} storage rate ($\Delta_t C_{ant}$) for the decades between 1990 and 2020 based on decadal data. Left column: whole water column, right column: only deep and bottom water masses. Top row: 1990–2000, middle: 2000–2010, bottom: 2010–2020. Only areas with a water depth larger than 200 m are considered. Station locations for the first period (1982–1994 in a, b, 1995–2005 in c, d and 2006–2013 in e, f) are marked in white, those for the second period (1995–2005 in a, b, 2006–2013 in c, d, 2014–2021 in e, f) in grey. Regions with differences smaller than the error range are stippled.
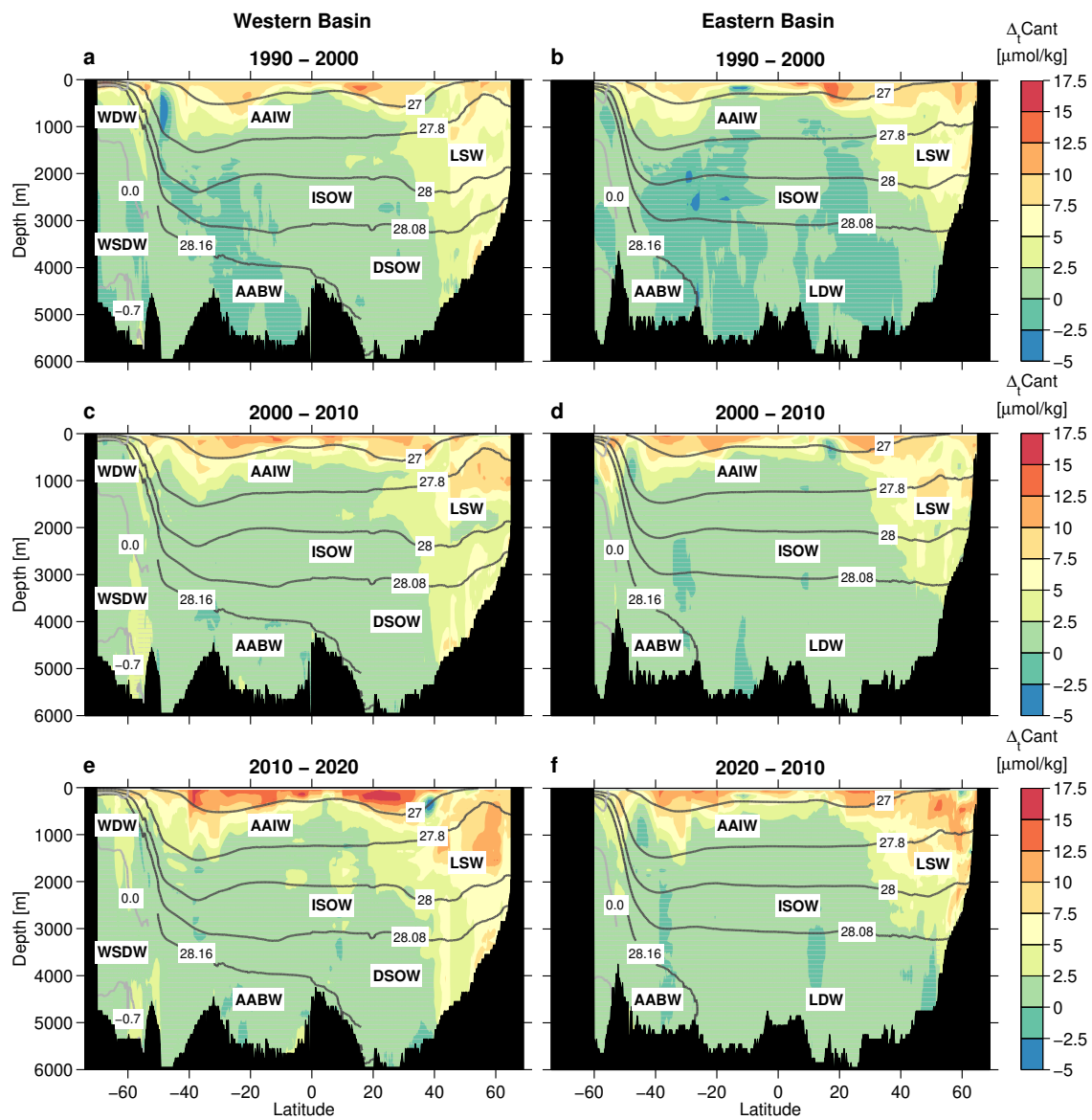
Figure 11. Zonal mean sections of C_{ant} concentration changes ($\Delta_t C_{ant}$) based on decadal data for the periods between 1990 and 2010. Left column: western basin; right column: eastern basin; top row: 1990–2000, middle: 2000–2010, bottom: 1990–2010. Regions with differences smaller than the error range are stippled. Contour lines are shown as in Fig. 2.
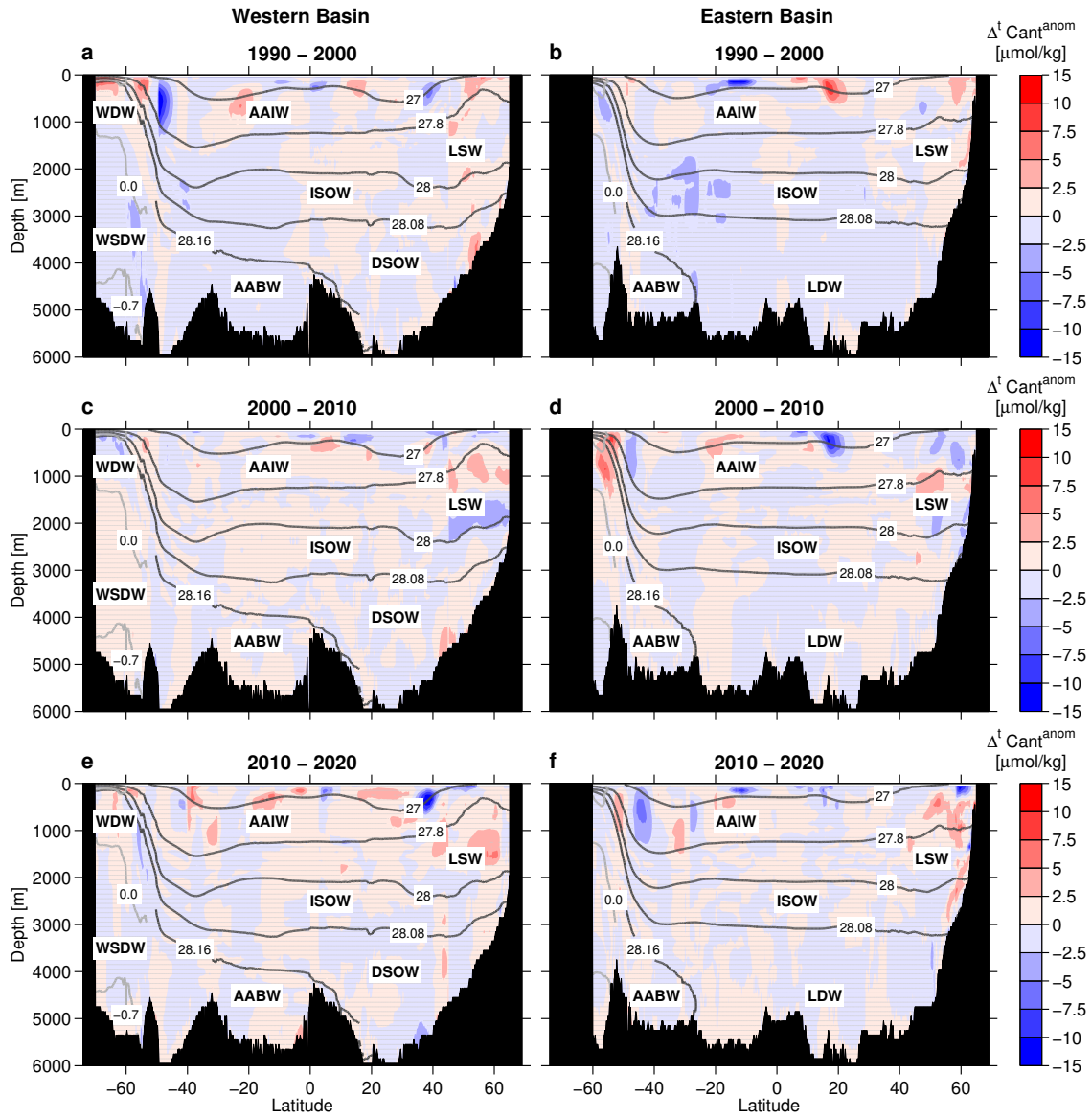
Figure 12. Zonal mean sections of $\Delta_t C_{ant}^{anom}$ (C_{ant} forecast based on tracer data from the first period minus C_{ant} based on tracer data from the second period). Left column: western basin, right column: eastern basin; top row: 1990–2000, middle: 2000–2010, bottom: 2010–2020. Regions with differences smaller than the error range are stippled. Contour lines are shown as in Fig. 2.
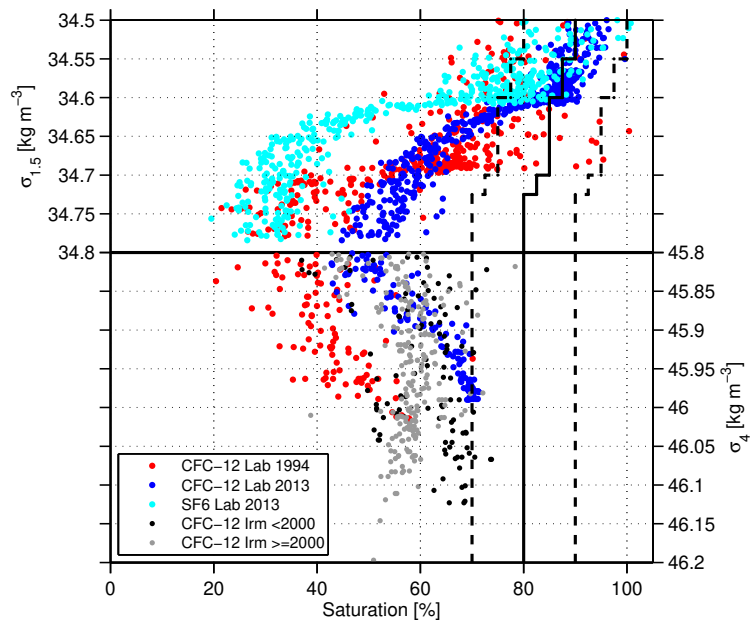
Figure B1. CFC-12 and SF_6 data below 500 m from the Labrador Sea (years 1994 and 2013) and the Irminger Sea (years prior to and after 2000), expressed as saturation with respect to the actual solubility equilibrium. Also shown is the assumed tracer saturation and the error margin of $\pm 10\%$.
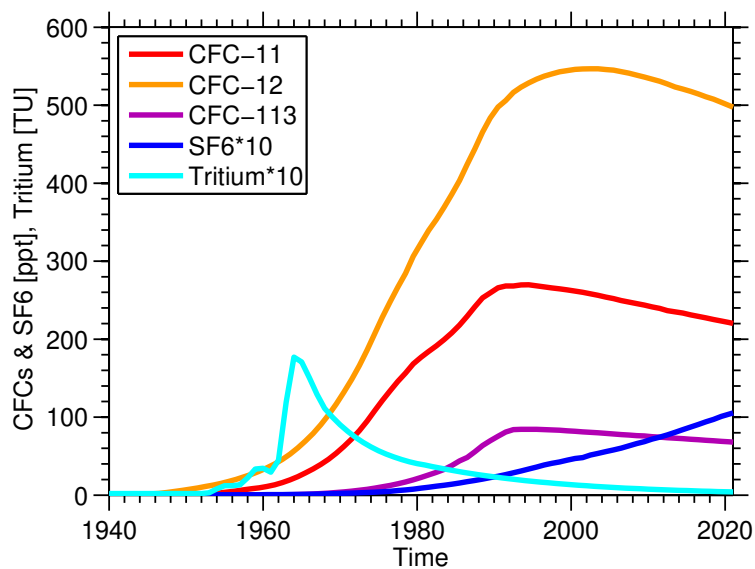
Figure C1. Time history of CFC-11, CFC-12, SF_6, and tritium for the northern hemisphere (the North Atlantic for tritium

.
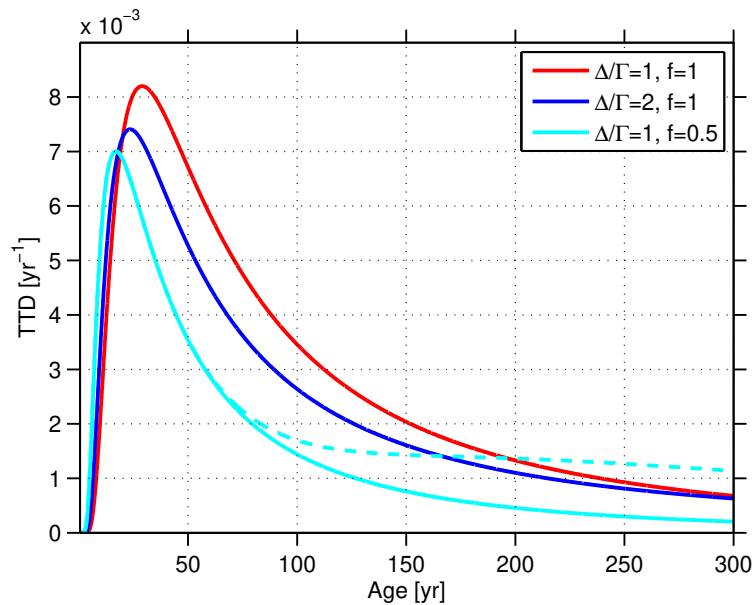
Figure D1. TTDs derived from an observed CFC-12 concentration of $0.4\,\mathrm{pmol\,kg^{-1}}$ in 2010, a CFC-saturation of 0.85, a potential tempera-ture of $\theta = 3^\circ\mathrm{C}$, and a salinity of S $= 34.9$y. Shown are TTDs for $f = 1$ and $\Delta/\Gamma = 1$ and $\Delta/\Gamma = 2$ respectively, as well as for $f = 0.5$ and $\Delta/\Gamma = 1$. For the latter case, also an assumed old TTD with with $\Gamma = 1000\,\mathrm{yr}$ and $\Delta = 500\,\mathrm{yr}$ is added (dashed cyan line).
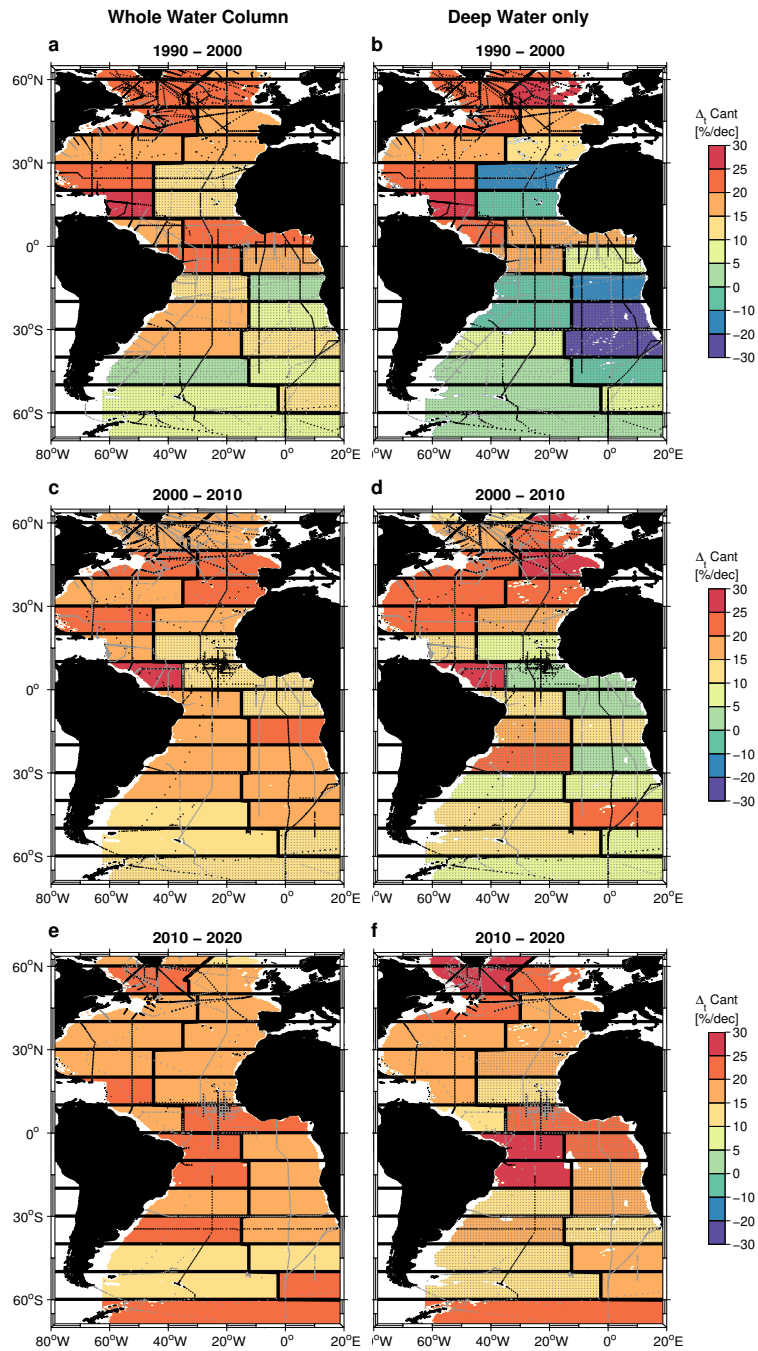
Figure E1. Left column: whole water column, right column: only deep and bottom water masses. Top row: 1990–2000, middle: 2000–2010, bottom: 2010–2020. Only areas with a water depth larger than 200 m are considered. Station locations for the first period (1982–1994 in a, b, 1995–2005 in c, d and 2006–2013 in e, f) are marked in white, those for the second period (1995–2005 in a, b, 2006–2013 in c, d and 2014–2021 in e, f) in grey. Regions with differences smaller than the error range are stippled.